TIFF: Gyrofluid Turbulence in Full-f and Full-k

Alexander Kendl

Institut für Ionenphysik und Angewandte Physik,

Universität Innsbruck, Technikerstrasse 25, 6020 Innsbruck, Austria *

arXiv:2306.02354v2 [physics.plasm-ph] 11 Jun 2023

Abstract

A model and code ("TIFF") for isothermal gyrofluid computation of quasi-two-dimensional interchange and drift wave turbulence in magnetized plasmas with arbitrary fluctuation amplitudes ("full-f") and arbitrary polarization wavelengths ("full-k") is introduced. The model reduces to the paradigmatic Hasegawa-Wakatani model in the limits of small turbulence amplitudes ("delta-f"), cold ions (without finite Larmor radius effects), and homogeneous magnetic field. Several solvers are compared for the generalized Poisson problem, that is intrinsic to the full-f gyrofluid (and gyrokinetic) polarization equation, and a novel implementation based on a dynamically corrected Fourier method is proposed. The code serves as a reference case for further development of three-dimensional full-f full-k models and solvers, and for fundamental exploration of large amplitude turbulence in the edge of magnetized plasmas.

*Electronic address: alexander.kendl@uibk.ac.at

I. INTRODUCTION: GYROFLUID MODELS AND POLARIZATION

Turbulence in magnetized plasmas, which is generally driven by ubiquitous gradients of density and temperature, is a subject of considerable interest and importance in fusion energy research with toroidal magnetic high-temperature plasma confinement experiments such as tokamaks and stellarators [1]. Models for instabilities and turbulence in magnetized plasmas are based on gyrokinetic, gyrofluid or fluid drift descriptions [2, 3].

Gyrofluid theory as a fluid-like model for the low-frequency dynamics of gyrocenter densities in magnetized plasmas including finite Larmor radius (FLR) effects has been pioneered in the late 1980s [4]. In the early 1990s collisionless Landau closure has been applied to derive three-dimensional gyrofluid models [5] for computations in slab [6] and toroidal geometry [7]. The approach was further generalized to electromagnetic models [8, 9]. Energetically consistent 6-moment electromagnetic gyrofluid equations with FLR effects have subsequently been systematically derived from the corresponding gyrokinetic theory [10, 11].

Gyrofluid theory has its place in the hierarchy of magnetized plasma models somewhere in between gyrokinetic and drift-reduced fluid theory [9–15]. The quality of a model of course not only depends on the rank within some straight hierarchy, but also on multiple secondary modelling assumptions that are introduced in any practical application and numerical simulation. Gyrofluids have the advantage over fluid theories to consistently model some kinetic effects such as finite Larmor radii or Landau damping. They do not depend on (Braginskii type) collisional closures, but collisional effects can be amended. Compared to gyrokinetic modelling of a 5-dimensional distribution function, the 3-dimensional gyrofluid moment models can be computationally much more efficient.

In "full-f" (a.k.a. "total-f") gyrofluid models [16–18], similar to full-f gyrokinetic models that evolve the total distribution function, no assumptions on the smallness of fluctuation amplitudes $f(\mathbf{x},t) = f_0(\mathbf{x}) + \tilde{f}(\mathbf{x},t)$ are made, instead of evolving only a small "delta-f" deviation $\tilde{f}$ from a static background equilibrium f_0 [19–25]. In fusion plasmas this is particularly relevant for the edge and scrape-off layer (SOL) regions, where large-amplitude blob or edge localized mode (ELM) filaments dominate the transport [26, 27].

The development of full-f gyrokinetic codes started a bit more than a decade ago (see, for example, refs. [15, 25, 28–37]), and often involves long-term development in large research groups or collaborations. All these (perpetually evolving) codes employ different levels of

secondary modelling assumptions and approximations, such as for geometry (full torus vs. flux tube; circular vs. X-point; core vs. edge/SOL), for polarization (linear vs. nonlinear), or for collision operators, electromagnetic effects, and (SOL and core) boundary conditions.

Full-f gyrofluid models are directly related to gyrokinetics, as they are usually obtained by taking appropriate fluid moments of the full-f gyrokinetic equations [18]. Therefore the difference between delta-f and full-f gyrofluid models involves the same choice of assumptions on the level of the gyrokinetic Lagrangian action, which in principle requires a consistent decision between either small perturbations but applicability for arbitary wave lengths, or arbitrary perturbation and flow amplitudes but restriction to long wave lengths [14, 16, 17].

For simulations of full-f gyrofluid models, over the last years two separate code implementations were developed alongside, which are both based on the same or similar model sets [18, 38], but use largely different numerical approaches: The modular open source code suite FELTOR ("Full-F ELectromagnetic code in TORoidal geometry") [39, 40] has been primarily developed and maintained by Wiesenberger and Held *et al.* [41–44]; and the code family TOEFL is being primarily developed by Kendl and includes the 2d code branch "TIFF", which is reported herein. The acronym TOEFL denotes "TOkamak Edge FLuid", and TIFF is "TOEFL In Full-f and Full-k". In its first (drift-Alfvén fluid in C/C++) implementation, TOEFL was largely tantamount to DALF [45] but in another language.

The 3d delta-f gyrofluid version T3P in the TOEFL set had been designed to be comparable with the GEM3 model and code by Scott [46] and Ribeiro [47], and was applied in refs. [48–51], and as 2d delta-f gyrofluid model reduction in refs. [50, 52, 53]. Full-f low-k 2d and 3d gyrofluid versions of TOEFL in the previous long wavelength approximation implementation, with otherwise similar numerics as employed here for TIFF, have already been applied in refs. [54–56]. These previous delta-f and full-f low-k simulations can serve as test cases for the implementation of the present full-f full-k model in its respective parameter limits. The dual FELTOR vs. TOEFL code development strategy allows cross-verification, but they for example also have optimized applicability for different geometries. Whereas FELTOR can be applied to full global 3d torus geometry, TOEFL is presently designed for locally field-aligned 3d flux-tube type toroidal simulation geometry.

What ever gyrofluid moment sets (such as thermal or isothermal, 2d or 3d) are treated in the codes, all gyrocenter densities are evolved and coupled to obtain the electric potential $\phi(\mathbf{x}, t)$ via the polarization equation, which is isomorphic to its full-f gyrokinetic equivalent,

and is nothing but the gyrocenter density ($N_s(\mathbf{x},t)$) formulation of quasi-neutrality, summing up all species (index s) charge and polarization densities.

Until recently, both full-f gyrofluid code families have treated the usual, consistent long-wavelength form of the full-f polarization equation [16–18]:

$$\sum_s \left[\boldsymbol{\nabla} \cdot \left(\frac{m_s N_s(\mathbf{x})}{B^2} \boldsymbol{\nabla}_\perp \phi(\mathbf{x}) \right) + q_s \, \mathrm{G}_{1s} N_s(\mathbf{x}) \right] = 0. \tag{1}$$

This can be re-cast into a generalized 2d Poisson equation:

$$\boldsymbol{\nabla} \cdot \varepsilon \, \boldsymbol{\nabla}_\perp \phi = \sigma \tag{2}$$

where $\varepsilon(\mathbf{x}) \equiv \sum_s m_s N_s(\mathbf{x})/B^2$, and $\sigma(\mathbf{x}) \equiv -\sum_s q_s \, \mathrm{G}_{1s} N_s(\mathbf{x})$. Here m_s is the mass and $q_s = Z_s e$ the charge of plasma species s with gyrocenter density N_s. The plasma species include electrons and at least one but often several ion species. In this present work only one main ion species (index $s = i$) in addition to the electrons (index $s = e$) is considered. The full-f gyrofluid generalization to multiple ion species has been discussed in refs. [55–57].

In the case of a pure e-i plasma, the polarization of the electrons can be neglected because $m_e \ll m_i$, so that $\varepsilon(\mathbf{x}) \approx m_i N_i(\mathbf{x})/B^2$. The gyrocenter densities N_s in σ are affected by gyro-averaging, which is denoted by the operator G_{1s}. This can be expressed as $\mathrm{G}_1(b_s) = \mathrm{G}_0^{1/2}(b_s)$ in wavenumber space with the gyro-screening operator $\mathrm{G}_{0s} \equiv I_0(b_s)e^{-b_s}$ for $b_s = (\rho_s k_\perp)^2$ [14]. This form (derived from velocity integration of the gyrokinetic pendant including Bessel functions) makes use of the modified Bessel function of the first kind I_0. The Larmor radius $\rho_s = \sqrt{T_s m_s}/(eB)$ of the particle species (s), with temperature T_s and mass m_s, normalizes the k_x and k_y wavenumber components in the 2d plane locally perpendicular to the magnetic field $\boldsymbol{B} = B\mathbf{e}_z$. The gyro-averaging operators can be efficiently approximated [14] by their Padé forms $G_0(b_s) \approx \Gamma_0(b_s) \equiv 1/(1+b_s)$ and $G_1(b_s) \approx \Gamma_1(b_s) \equiv 1/(1+b_s/2)$.

The full dynamical nonlinearity $\boldsymbol{\nabla} \cdot \varepsilon(x,y,t) \, \boldsymbol{\nabla}_\perp \phi$ in the long-wavelength polarization equation is here retained. Most full-f gyrokinetic implementations so far approximate this term by using either only radial variations of the static background $\varepsilon_0(x)$, or completely linearise it to $\sim \varepsilon_0 \boldsymbol{\nabla}_\perp^2 \phi$ and so neglect spatial and temporal variations in the polarization.

However, the general delta-f form of the polarization equation

$$\sum_s \left[\frac{q_s e N_0}{T_s} \left(\Gamma_{0s} - 1 \right) \phi + q_s N_0 \, \Gamma_{1s} \frac{\tilde{N}_s}{N_0} \right] = 0, \tag{3}$$

for small perturbations $\tilde{N}_s$ on a reference background density N_0, differs from this linearised long-wave length polarization by an additional FLR contribution proportional to the Larmor radius ρ_s, and only agrees in lowest order Taylor expansion in $b = (\rho_s k_\perp)^2$ [14]:

$$\begin{aligned} \frac{e^2 Z_s N_0}{T_s} \left(\Gamma_{0s} - 1\right) \phi \; &= \; \frac{m_s Z_s N_0}{B^2} \frac{\boldsymbol{\nabla}_\perp^2}{1 - \rho_s^2 \boldsymbol{\nabla}_\perp^2} \phi \\ &\neq \; \frac{m_s Z_s N_0}{B^2} \boldsymbol{\nabla}_\perp^2 \phi \equiv \varepsilon_0 \boldsymbol{\nabla}_\perp^2 \phi \end{aligned} \tag{4}$$

In any case consistency throughout the equations has to be ensured, for example in full-f models by keeping E-cross-B energy terms in the generalised potential [14, 18]. Computation of delta-f gyrofluid turbulence with the exact model in comparison to the delta-f long-wavelength approximation such as in eq. (5) show that the differences can be rather pronounced. This has motivated the development of a consistent arbitrary wavelength full-f gyrofluid polarization model [58]. A first implementation of this "full-f full-k" model in the code FELTOR and application to simulation of interchange driven "blob" perturbations in a magnetized plasma is presented by Held and Wiesenberger in ref. [59]. The results therein clearly show the relevance of arbitrary wave length polarization for interchange drift modes.

In the present work, an independent code implementation (TIFF) of the "full-f full-k" model and application to 2d drift instabilities and turbulence is given. In the respective interchange blob mode limit, the results are cross-verified with the recent FELTOR code results. Different solvers for the underlying generalized Poisson problem are compared. An efficient solver based on a dynamically corrected Fourier method is proposed and tested.

II. FULL-F FULL-K 2D GYROFLUID TURBULENCE MODEL

The arbitrary wave length full-f model derived in ref. [58] and first applied by Held and Wiesenberger in ref. [59], is in the following implemented in a form which also includes the full-f formulation of the gyrofluid generalization [43, 44] of the quasi-2d (modified) Hasegawa-Wakatani (HW) drift wave turbulence model [60, 61].

A. Gyrocenter density equations

The set of isothermal full-f full-k gyrofluid equations is based on dynamical evolution equations of the gyrocenter densities for each species s in the general form of a continuity

equation:

$$\partial_t N_s + \boldsymbol{\nabla} \cdot (N_s \boldsymbol{U}_s) = 0. \tag{5}$$

The velocities $\boldsymbol{U}_s = \boldsymbol{U}_E + \boldsymbol{U}_B + \boldsymbol{U}_\parallel$ include the gyro-center E-cross-B drifts $\boldsymbol{U}_E = (1/B^2)\boldsymbol{B} \times \boldsymbol{\nabla}_\perp \phi_s$, the gradient-B drifts $\boldsymbol{U}_B = (T_s/q_s B^2)\boldsymbol{B} \times \boldsymbol{\nabla}_\perp \ln(B/B_0)$, and parallel velocities $\boldsymbol{U}_\parallel$. In contrast to the corresponding fluid continuity equation for particle densities, the gyrofluid formulation for gyrocenter densities does not contain polarization drifts, whose effects are covered by the relation of the gyrocenter densities within the polarization equation for the electric potential ϕ. The resulting set of equations can be seen as a variation of the vorticity-streamfunction formulation for a 2D Euler fluid model. The electric potential here takes the role of a streamfunction for the advecting E-cross-B velocity.

The gyrofluid potentials $\phi_s = \Gamma_{1s}\phi + \Psi_s$ in the E-cross-B drift $\boldsymbol{U}_E$ include the gyro-average part, and the consistent full-f full-k form [58] of the polarization contribution through the E-cross-B energy as $\Psi_s = (m/2qB^2)|\nabla_\perp \sqrt{\Gamma_0}\phi|^2$. For electrons $\phi_e \approx \phi$ can be used because of the small mass ratio and associated small Larmor radius in comparison to ions. The potential ϕ is retrieved from solution of the polarization equation.

B. Polarization equation

The consistent arbitrary wavelength full-f polarisation equation has been derived in ref. [58] and is used here in isothermal (constant gyroradius) form as in ref. [59]:

$$\sum_s q_s N_s - \boldsymbol{\nabla} \cdot (\boldsymbol{P}_1 + \boldsymbol{P}_2) = 0, \tag{6}$$

where the polarization densities are given as

$$\boldsymbol{P}_1 = -(1/2) \sum_s q_s \boldsymbol{\nabla}_\perp \Gamma_1 \rho_s^2 N_s, \tag{7}$$

$$\boldsymbol{P}_2 = -\sum_s \left(\sqrt{\Gamma_0} \frac{q_s N_s}{\Omega_s B} \sqrt{\Gamma_0} \boldsymbol{\nabla}_\perp \phi \right). \tag{8}$$

Here, in the (isothermal) constant gyroradius approximation the Γ_1 and $\sqrt{\Gamma_0}$ operators are self-adjoint, and may for example be evaluated efficiently in $\boldsymbol{k}$ space. The general form for $\rho_s = \rho_s(\boldsymbol{x})$ is given in ref. [58].

For the present implementation in the code TIFF only one ion species (e.g. Deuterium) is treated, and the electron polarization is neglected. The full-f full-k polarization equation

then can be re-written as:

$$\boldsymbol{\nabla} \cdot \sqrt{\Gamma_0}\varepsilon_i\sqrt{\Gamma_0}\boldsymbol{\nabla}_\perp\phi = \sigma \tag{9}$$

where $\sigma(\mathbf{x}) \equiv -\sum_s Z_s\Gamma_{1s}N_s(\mathbf{x})$, with Γ_0 (here for ions only) and Γ_{1s} given in second order accurate Padé approximation [58, 59], as given above, and $\varepsilon_i(\mathbf{x}) = m_iN_i(\mathbf{x})/B^2$. In the constant gyroradius (isothermal) case the $\sqrt{\Gamma_0}$ operators commute with the $\boldsymbol{\nabla}$ operators, so that also $\sqrt{\Gamma_0}\boldsymbol{\nabla} \cdot \varepsilon_i\boldsymbol{\nabla}_\perp\sqrt{\Gamma_0}\phi = \sigma$ holds. By defining $\phi_G \equiv \sqrt{\Gamma_0}\phi$ and $\sigma_G \equiv \sqrt{\Gamma_0}^{-1}\sigma$, the arbitrary wave length polarization eq. (9) can again be re-cast into the usual form of a generalised 2d Poisson equation as $\boldsymbol{\nabla} \cdot \varepsilon_i\boldsymbol{\nabla}_\perp\phi_G = \sigma_G$. This allows to re-use common solvers (see Appendix) for this type of problem to obtain ϕ_G and thus ϕ from known ε_i and σ. For variable gyroradii $\rho_s(\mathbf{x})$ or multiple polarizable species other forms of numerical solvers may have to be implemented.

The isothermal gyrofluid model consists basically of eqs. (5) for both electron and ion gyrocenter densities, which are coupled via eq. (9). The numerical implementation in non-dimensional form is achieved by the usual drift normalization. For this purpose the flux divergence contributions in eqs. (5) are first restated.

C. Divergence of perpendicular fluxes

The divergence of the E-cross-B flux part in eq. (5) provides the advective derivative term $\boldsymbol{U}_E \cdot \boldsymbol{\nabla}N_s = (1/B)[\phi_s, N_s]$ as the primary turbulent nonlinearity, and in the case of an inhomogeneous magnetic field the "curvature" term $N_s\boldsymbol{\nabla} \cdot \boldsymbol{U}_E = N_s[\ln B, \phi_s]$. (Side note: this contribution is here referred to as "curvature" although in a strict sense a quasi-2d model with straight magnetic field lines $\boldsymbol{B} = B(x)\boldsymbol{e}_z$ only has a gradient-B effect; however, in a toroidal system both curvature and gradient-B contributions occur in combination, and can be treated similarly within joint 3d expressions in (gyro-) fluid models if $T_\parallel \approx T_\perp$.)

The 2d advective drift operators $(\boldsymbol{e}_z \times \boldsymbol{\nabla}\phi_s) \cdot \boldsymbol{\nabla}f \equiv [\phi_s, f]$ are here expressed in Poisson bracket notation, where $[a, b] = (\partial_x a)(\partial_y b) - (\partial_x b)(\partial_y a)$. The 2d gyrofluid potential field thus has the meaning of a stream function for the turbulent E-cross-B flows.

The divergence of the gradient-B flux gives the diamagnetic curvature term $\boldsymbol{\nabla} \cdot (N_s\boldsymbol{U}_B) = (N_sT_s/q_sB)[\ln B, N_s]$. In contrast to delta-f models, these terms are not linearized and the full gyrocenter densities are in this form retained as multipliers to the Poisson brackets.

D. Parallel closure

In the present quasi-2d model the parallel velocity $\boldsymbol{U}_\parallel$ contribution can be approximated by means of the Hasegawa-Wakatani closure [60]. From the full-f electron parallel momentum equation [18] in the quasi-stationary limit a relation in the form of a generalized Ohm's law is obtained as $e\eta_\parallel J_\parallel = T_e\nabla_\parallel \ln N_e - e\nabla_\parallel\phi$. With $J_\parallel \approx -eN_e\boldsymbol{U}_{\parallel e}$, by assumption of a Spitzer resistivity $\eta_\parallel = 0.51 m_e\nu_e/(n_e e^2)$, and applying that the electron gyrocenter density $N_e \approx n_e$ can be approximated well by the electron particle density n_e, an expression for the term $\boldsymbol{\nabla}\cdot(N_e\boldsymbol{U}_{\parallel e}) \equiv -\Lambda_{ce}$ in eq. (5) can be obtained [43]. The ion velocity contribution in the parallel response can be neglected because of the high ion inertia compared to electrons.

For this purpose a full-f non-adiabatic coupling parameter $\alpha \equiv T_e k_\parallel^2/(\eta_\parallel e^2 n_0\omega_0) = n_e T_e k_\parallel^2/(0.51 m_e\nu_e n_0\omega_0)$ can be defined for a selected parallel wavenumber $k_\parallel$ with $\omega_0 = eB/m_i$. The electron collision frequency ν_e is in principle proportional to n_e, inversely to $T_e^{3/2}$, and to the (in general density and temperature dependent) Coulomb logarithm. The usual approximation of a constant Coulomb logarithm is applied here, and in the present isothermal model only the density dependence $\nu_e(n_e) \sim n_e \sim N_e$ needs to be discussed [43]: in the classical delta-f fluid HW model the collision frequency is assumed constant, so that α is a free constant parameter, whereas for the present full-f model the dependence is kept as $\alpha = N_e\alpha_0$. The final non-adiabatic "ordinary" HW drive term for electrons in the full-f form [43] is $\Lambda_c = \alpha n_0\omega_0[(e\phi/T_e) - \ln(N/\langle N\rangle)]$. The angled brackets denote a zonal average, which in the present 2d geometry amounts to averaging in the y direction.

E. Normalization to dimensionless form

The preceding evaluation of perpendicular and parallel fluxes gives the (still dimensional) density equations (5) alternatively as

$$\partial_t N_s + \frac{1}{B}[\phi_s, N_s] + \frac{N_s}{B}[B,\phi_s] + \frac{N_s T_s}{q_s B^2}[B, N_s] = \Lambda_{cs}, \tag{10}$$

where the nonadiabatic coupling term Λ_{cs} only is contributing for electrons ($\Lambda_{ci} \equiv 0$).

Time t in the partial time derivative is normalized with respect to $L_\perp/c_0$, where $c_0 = \sqrt{T_e/m_i}$ is the thermal speed, and $L_\perp$ is a "typical" perpendicular length scale. For local pressure gradient driven systems this is usually set equal to the background gradient length, here $L_\perp \equiv L_n = |\partial_x \ln n_0(x)|^{-1}$, so that temporal normalization relates to the diamagnetic

drift frequency $\omega_* = c_0/L_n$. For global gradient driven systems often the minor torus radius $L_\perp \equiv a$ is rather used. In case of model systems with absent background gradient, such as for interchange driven "blob" setups, $L_\perp \equiv \rho_0 \equiv \sqrt{T_e m_i}/(eB)$ is chosen as the drift scale, and time normalization is related to the ion gyration frequency $\omega_0 = c_0/\rho_0$. These choices can be set by specifying $\delta \equiv \rho_0/L_\perp$ as a free input parameter.

The perpendicular spatial derivatives in x and y are always normalized with respect to ρ_0, so that $\hat{\partial}_t \equiv (L_\perp/c_0)\partial_t$, and $\{\cdot,\cdot\} \equiv \rho_0^2[\cdot,\cdot]$. Densities and the magnetic field are normalized to reference quantities $\hat{N} = N/N_0$ and $\hat{B} = B/B_0$, respectively, and the electric potential as $\hat{\phi} \equiv e\phi/T_e$. Temperature ratios are defined as $\tau_s \equiv T_s/(T_e Z_s)$.

Dividing eq. (10) by N_s and multiplying with $L_\perp/c_0$ gives:

$$\hat{\partial}_t \ln \hat{N}_s + \frac{1}{\hat{B}\delta}\{\hat{\phi}_s, \ln \hat{N}_s\} = \hat{\Lambda}_{cs} + \hat{\Lambda}_{Bs}, \tag{11}$$

The normalized dissipative coupling term $\hat{\Lambda}_{ce} \equiv (L_\perp/c_0)(\Lambda_{ce}/\hat{N}_e) = \hat{\alpha}[\hat{\phi} - \ln(N_e/\langle N_e\rangle)]$, with $\hat{\alpha} = \delta(L_\perp/L_\parallel)^2(\omega_{ce}/\nu_e)(\hat{k}_\parallel^2/0.51)$ as a free parameter, appears only in the electron equation, and $\Lambda_{ci} \equiv 0$. The "modified HW" model for toroidally more concordant zonal flow treatment requires to use $\hat{\Lambda}_{ce} = \hat{\alpha}[(\hat{\phi} - \langle\hat{\phi}\rangle) - (\ln N_e - \langle \ln N_e\rangle)]$ instead [43]. In these forms both are directly consistent with their respective common delta-f limits ($\ln N_e \to \tilde{N}_e/N_0$).

In the present quasi-2d setup it is assumed that the magnetic field has locally only a weak dependence in $B(x)$, so that $\delta^{-1}\{\ln B, f\} \equiv -\kappa\hat{\partial}_y f \equiv -\mathcal{K}(f)$, with $\kappa \equiv -\delta^{-1}(\hat{\partial}_x \ln B)$ taken as a constant parameter. This is also consistent with the assumption of a constant gyroradius, throughout the computational domain which is supposed to have a radial extension $L_x \ll R$ much smaller than the major torus radius R. For global simulations across the whole torus cross section this condition would need to be relaxed.

The x direction is here chosen to be local radially outwards on the outboard midplane side of a torus (compare Fig. 1), where $\kappa > 0$, and $\hat{B}(x) \approx 1 - \kappa x \approx 1$ is weakly decreasing with x. This gives $\hat{\Lambda}_{Bs} \equiv \mathcal{K}(\hat{\phi}_s) + \tau_s\mathcal{K}(\ln \hat{N}_s)$. The curvature strength can be evaluated as $\kappa \approx 2\rho_0/R$. The temperature ratio is always $\tau_e = -1$ for electrons, and a free parameter for ions in the order of $\tau_i \sim +1$. The ion temperature ratio τ_i thus controls the FLR effects, and in addition here also the ion diamagnetic contribution to gradient-B (interchange) drive for inhomogeneous magnetic fields ($\kappa \neq 0$).

The formulation in terms of $\ln \hat{N}$ as the dynamical variable for the time evolution of densities ensures that $\hat{N}$ is always positive definite, which is a requirement for the solution

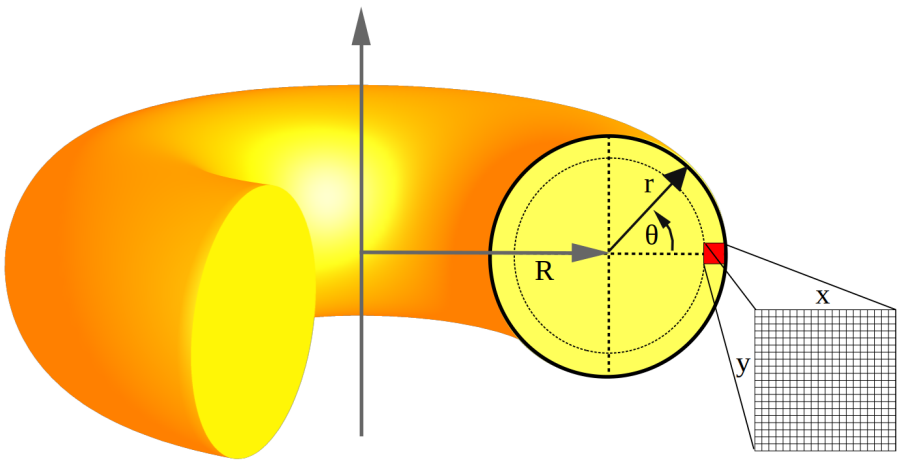


FIG. 1: The TIFF simulation domain is set in a small 2d locally rectangular (x, y) area in the poloidal cross-section of a torus, such as of a tokamak fusion plasma. The magnetic field direction is locally perpendicular to the (x, y) plane. The advecting fluid-like drift velocities in this perpendicular direction are responsible for instabilities and plasma turbulence in the presence of (radial) pressure gradients and of magnetic field inhomogeneity.

of the generalized Poisson equation, and directly reduces to the delta-f density equation as $\ln \hat{N} \approx \hat{N} - 1 = (N_0 + \tilde{N})/N_0 - 1 = \tilde{N}/N_0$ for small relative fluctuation amplitudes $\hat{N} \ll N_0$.

F. Normalized polarization

In a quasi-neutral magnetized plasma under fluid drift ordering, the divergences of the above perpendicular and parallel fluxes are balanced by the divergence of the polarization drift. In gyrofluid and gyrokinetic models this is taken into account by enforcing quasi-neutrality $\sum_s q_s n_s \equiv 0$, and replacing the particle densities n_s herein in terms of their respective gyrocenter and polarization densities, with the need to determine a consistent electric potential as a result.

The polarization equation (9) is made non-dimensional by applying the same normalizations as above, which results in $\hat{\boldsymbol{\nabla}} \cdot \sqrt{\Gamma_0}\hat{\varepsilon}_i\sqrt{\Gamma_0}\hat{\boldsymbol{\nabla}}_\perp\phi = \hat{\sigma}$, with $\hat{\varepsilon}_i = \hat{N}_i/\hat{B}^2$ and $\hat{\sigma} = -\sum_s Z_s\Gamma_{1s}\hat{N}_s(\mathbf{x})$. The gyration operators are already dimensionless by definition.

G. Selection of edge and scrape-off-layer model scenarios

The usual applications for quasi-2d simulations of nonlinear drift dynamics in magnetized plasmas are, for example, fundamental studies on either (a) gyrofluid turbulence and zonal flows with FLR effects, or on (b) FLR effects on interchange dynamics of warm "blob" perturbation propagation. Both cases are commonly treated in separate studies, where for (a) $\Lambda_{Bs} \equiv 0$, and instead for (b) $\Lambda_c \equiv 0$ is set respectively, for better separability and understanding of basic underlying mechanisms.

"Blob" transport is regarded as most relevant in the scrape-off-layer (SOL) of fusion plasmas. Studies with single or few seeded blobs are important to reveal fundamental mechanisms, but in tokamaks blobs are presumed to be generated rather "randomly" around the separatrix, so that turbulent drift wave vortices and zonal flow effects from the closed field line (CFL) edge region will play a large role for consistent studies of "blobby" (intermittent) SOL transport. Several 2d fluid codes (for example as in refs. [62–64]) take into account both drift wave and interchange effects and different background conditions by assigning two regions, that are defined by a "separatrix" location x_s within the same 2d computational domain.

An additional effect that should be taken into account in the SOL region is sheath coupling of the open field lines with limiter or divertor material walls. This effect intrinsically includes parallel kinetics along the magnetic field direction. Gyrokinetic, gyrofluid and fluid models for sheath coupling conditions may be approximated under assumption of Bohm conditions. Any perpendicular 2d fluid-type approximation will likely miss relevant physics here, but can in principle be included also in the present 2d full-f gyrofluid model. For test purposes presently a (partly inconsistent) sheath instability "toy model" is optionally included in the TIFF code with additional coupling terms added to the right hand side of eq. (11), which needs further improvement before any application. For example, a 2d delta-f form of the gyrofluid sheath coupling terms was introduced by Ribeiro [47], as $N_e\hat{\Lambda}_{Se} \to \gamma_D[(1 + \Lambda_D)\tilde{N}_e - \hat{\phi}]$ and $\hat{\Lambda}_{Si} \to \gamma_D\tilde{N}_e$, with sheath coupling parameter γ_D as defined in ref. [47], and $\Lambda_D = \log(\sqrt{m_i/2\pi m_e})$. This model add-on in principle will allow to examine simplified edge-SOL coupled turbulence and flow dynamics including turbulent generation of SOL blobs, once a consistent full-f full-k sheath coupling term is derived and implemented in the future. For this reason, the present paper only discusses simulations without sheath coupling.

All coupling terms $\hat{\Lambda}$ on the right hand side of eq. (11) are then selectively only applied in the respective regions of interest, for example formally by multiplication with Heaviside type step functions $\lambda(x_s)$ for a given relative separatrix position $0 \leq (x_s/L_x) \leq 1$.

Application cases and systematic physics studies will be presented elsewhere. Here the focus is on introduction of the code TIFF and its presently underlying model as a reference for later applications and further developments, such as toroidal geometry and inclusion of thermal and electromagnetic dynamics in a (field-aligned) 3d extension. A main aspect here is also on introduction and testing of an efficient dynamically corrected Fourier solver for the generalized Poisson problem in the polarization.

III. NUMERICAL SOLUTION ALGORITHM

The normalized equations solved in the TIFF code are:

$$\hat{\partial}_t \ln \hat{N}_e + \{\hat{\phi}, \ln \hat{N}_e\} = \lambda_B \hat{\Lambda}_{Be} + \lambda_S \hat{\Lambda}_{Se} + \lambda_c \hat{\Lambda}_c \tag{12}$$

$$\hat{\partial}_t \ln \hat{N}_i + \{\hat{\phi}_i, \ln \hat{N}_i\} = \lambda_B \hat{\Lambda}_{Bi} + \lambda_S \hat{\Lambda}_{Si} \tag{13}$$

$$\hat{\boldsymbol{\nabla}} \cdot \hat{\varepsilon}_i \hat{\boldsymbol{\nabla}}_\perp \hat{\phi}_G = \hat{\sigma}_G \tag{14}$$

The general procedure for solution of this set of equations is as follows:
(#1) Specify $\hat{N}_e(\boldsymbol{x})$ and $\hat{N}_i(\boldsymbol{x})$ on an equidistant grid in a 2d rectangular (x, y) domain, either as initial condition, or subsequently updated in each time step by eqs. (12-13).
(#2) Compute $\hat{N}_{Gi} \equiv \Gamma_{1i} \hat{N}_i$. The constant gyroradius assumption allows to evaluate all gyro-averaging operations efficiently in $\boldsymbol{k}$ space, here $\hat{N}_{Gi}(\boldsymbol{k}) = \hat{N}_i(\boldsymbol{k})/(1 + \tau_i \hat{k}^2/2)$. In the TIFF code presently the 2d discrete Fourier transform from the FFTW3 library [65] is used for transformations between $\boldsymbol{k}$ and $\boldsymbol{x}$ space representations.
(#3) Apply boundary conditions (see next section) on $\hat{N}_e$, $\hat{N}_i$ and $\hat{N}_{Gi}$.
(#4) Prepare the input functions to eq. (14) as $\hat{\sigma}_G = \sqrt{\Gamma_0}^{-1} \hat{\sigma} = \sqrt{1 + \tau_i \hat{k}^2}\ \hat{\sigma}$ with $\hat{\sigma} = \hat{N}_e - Z_i \hat{N}_{Gi}$, and $\hat{\varepsilon}_i = \hat{N}_i / \hat{B}^2$.
(#5) Obtain $\hat{\phi}_G$ from eq. (14) with one of the solvers discussed in the Appendix.
(#6) Compute the electric potential from $\hat{\phi} = \sqrt{\Gamma_0}^{-1} \hat{\phi}_G$ also via $\boldsymbol{k}$ space.
(#7) Compute the gyrofluid ion potential $\hat{\phi}_i = \Gamma_{1i} \hat{\phi} + |\hat{\nabla}_\perp \hat{\phi}_G|^2 / (2\hat{B}^2)$.
(#9) Update $\hat{N}_e$ and $\hat{N}_i$ in time through eqs. (12-13) and return to step (#1).

The time step update (#9) first requires evaluation of the advective Poisson brackets and all coupling terms $\hat{\Lambda}$. The brackets $\{\cdot,\cdot\}$ are here presently solved with the energy and enstrophy conserving (but not shock capturing) fourth order Arakawa scheme [66, 67].

In $\hat{\Lambda}_{Bs}$ the curvature operators $\mathcal{K}(f) = \kappa\hat{\partial}_y f$ are evaluated by (fourth order) centered finite differencing over the (periodic) y direction. Evaluation of $\hat{\Lambda}_{Ss}$ and $\hat{\Lambda}_{ce}$ are straightforward. $\hat{\Lambda}_{ce}$ includes calculation of zonal averages $\langle f\rangle(x) = (1/n_y)\sum_j f_{i,j}$, which on a 2d rectangular local grid simply requires summation over all n_y grid points j of the y direction.

Time step updating of $f \equiv \ln \hat{N}_s$ in the form $\partial_t f = F$ here uses a fourth order accurate three-step Adams-Bashforth method with Karniadakis weights [68]:

$$\begin{aligned} f^{(t+1)} &= c_0 f^{(t)} - c_1 f^{(t-1)} + c_2 f^{(t-2)} \\ &+ c_F \Delta t \left[3F^{(t)} - 3F^{(t-1)} + F^{(t-2)} + \hat{\Lambda}_\nu^{(t)} \right] \end{aligned} \tag{15}$$

where $c_0 = 18/11$, $c_1 = 9/11$, $c_2 = 2/11$ and $c_F = 6/11$. The (normalized) time step size Δt has to be small enough for CFL stability. For further numerical stabilization of the otherwise explicit scheme an artificial sub-grid type viscosity term Λ_ν is added. For this a hyperviscosity $\hat{\Lambda}_\nu = -\nu_4 \hat{\boldsymbol{\nabla}}^4 \ln \hat{N}_s$ is here applied. The coefficient $0 \leq \nu_4 \ll 1$ is heuristically chosen to prevent grid instability at smallest scales, as a sink for the nonlinear direct vorticity cascade, and to (slightly) damp out Gibbs type noise that can appear at under-resolved strong gradients due to the not shock capturing nature of the Arakawa discretization. The value of $\nu_4(h)$ needs to be adapted when spatial grid resolution h is changed to achieve optimum results. If desired, for example for comparability to other code implementations, an ordinary "physical" viscous diffusion term $\hat{\Lambda}_\mu = +\mu(\hat{\boldsymbol{\nabla}}^2 \hat{N}_s)/\hat{N}_s$ could be added to the right hand side of eqs. (12-13). For usual application of the gyrofluid model to hot fusion edge plasmas the actual viscosity μ in general would be too small to be resolved efficiently by direct numerical simulation.

For solution of the generalized Poisson problem as in step (#5) of the outlined algorithm, presently three methods are implemented in TIFF as described in more detail in the Appendix: An iterative preconditioned conjugate gradient (PCG) solver, an iterative red-black successive over-relaxation (SOR) solver, and a novel dynamically corrected Fourier (DCF) solver. All solvers make use of the results for $\phi^{(t-1)}$ and $\phi^{(t-2)}$ of the previous time steps, either for extrapolated initialisation of the iterative schemes, or for the (therefore denoted "dynamical") correction of the approximate Fourier method. The DCF method leads to

predictable run times of the generalized Poisson problem, that only depend on the grid size but not on other simulation parameters, whereas the number of iterations and run time can vary significantly for the PCG and SOR solvers for any specified accuracy, in particular when densities (and thus $\hat{\varepsilon}_i(\mathbf{x})$) are strongly inhomogeneous.

IV. INITIAL AND BOUNDARY CONDITIONS

Initially the gyrocenter density $\hat{N}_i(x, y)$ and $\hat{N}_e(x, y)$ fields have to be specified. For full-f initial background profiles a radially exponential decline is set, each with $\hat{N}_0(x) = \hat{N}_L \exp(-x/d)$ for $d = L_p/\ln(n_L/N_p)$. Here $L_p = x_s$ denotes either the width of the pedestal region if a separatrix at $x_s < L_x$ is applied, or the width L_x of the whole x domain if no SOL region is treated. The initial $\ln \hat{N}_s$, profiles (and in its limit the delta-f $\tilde{N}$ profiles) are thus linear. On top of this initial background, either single perturbations, such as a Gaussian density blob, or a pseudo-random "bath" of modes, is added with a given amplitude. The initial ion gyrocenter density is either set equal to the electron density, or a "vorticity free" initialisation with $\hat{N}_i = \Gamma_1^{-1}\hat{N}_e$ is used so that $\hat{\sigma} = 0$.

Boundary conditions are applied in several instances: on density profiles in order to maintain a background gradient if required, for the intrisic boundary value problem of the Poisson equation, for solution of the gyro operators in $\boldsymbol{k}$ space, and on finite difference operators in $\boldsymbol{x}$ space. The "poloidal" y direction is assumed periodic. The box length L_y in units of ρ_0 has to be chosen much larger than typical perpendicular correlation lengths for turbulence simulations, or much larger than blob or vortex scales for simulation of such structures, in order to minimize self-interaction effects across the periodic y boundary.

A. Density profile boundary conditions

Density profiles could be maintained by specifying source terms $\hat{\Lambda}_Q(x)$ around the inner ($x = 0$) radial boundary and sink terms around the outer ($x = L_x$) boundary.

The presently considered application scenarios are for example a full-f gyrofluid generalization of HW turbulence simulations, or seeded blob simulations on a (usually) constant background density. For comparability to common delta-f implementations of these scenarios it is adequate to maintain an average density profile by prescribing fixed boundary densities

$\hat{N}(x=0) \equiv \hat{N}_L$ and $\hat{N}(x=L_x) \equiv \hat{N}_R$, while the full densities may still self-consistently evolve in between. Seeded blob simulations could for example use $\hat{N}_L = \hat{N}_R = 1$.

"Classical" fluid or delta-f gyrofluid HW turbulence simulations usually decouple a constant background gradient in the advective derivative as $\delta^{-1}\{\phi, \tilde{N} + N_0(x)\} = \delta^{-1}\{\phi, \tilde{N}\} + g\hat{\partial}_y\phi$ with a gradient parameter $g = \delta^{-1}(\rho_s/L_n)$. For the "diamagnetic drift frequency" normalization of time this amounts to $g = 1$, but g could also be kept as a free parameter [61]. The restriction in delta-f fluid or gyrofluid simulations to small fluctuations that are decoupled from the background profile enables the use of periodic boundary conditions in x on $\tilde{N}$ and ϕ. This is not feasible any more for both delta-f or full-f simulations with global profile evolution.

If δ is specified as an input parameter, then this needs to be chosen consistently with the required density boundary values for profile driven simulations as $\delta = (\hat{N}_L - \hat{N}_R)/L_x$. When for example the radial domain size is $L_x = 64$ in units of ρ_0, then setting $\hat{N}_L = 1 + 0.5$ and $\hat{N}_R = 1 - 0.5$ specifies $\delta = 1/64 \approx 0.015$.

The typical experimental tokamak edge steep density gradient pedestal regions, which are the usual scenario of interest for HW model simulations, have widths in the order of around 50 to 100 ρ_0 and drift scales $\delta \sim \mathcal{O}(10^{-2})$.

B. Parametric transition to delta-f limit within full-f equations

Specification of the density boundary in this way allows for a consistent treatment and verification of the delta-f limit of small perturbation amplitudes on large relative background densities within the full-f code. For gradient driven turbulence this can be achieved by reducing all of the background variation, drift scale, and initial perturbation amplitudes by the same small factor ϵ. For example, setting $\hat{N}_L = 1 + \epsilon \cdot 0.5$ and $\hat{N}_R = 1 - \epsilon \cdot 0.5$ for the same box size of $L_x = 64$ gives $\delta \approx \epsilon \cdot 0.015$. When initial (for example blob) perturbation amplitudes $\epsilon \cdot \Delta n$ are in the full-f model chosen smaller by the same factor (for example $\epsilon = 1/100$) as in a corresponding delta-f code (with initial amplitude Δn), then this corresponds to the respective delta-f setup and enables a direct comparison (and code cross-verfication) of this limit when $\epsilon \to 0$.

C. Radial boundary density condition

It is desirable to reduce density fluctuations and maintain zero vorticity and/or flows on narrow inner and outer radial boundary layers. The boundary layer region of "width" $L_\beta \ll L_x$ is here defined by a function $\beta(\hat{x}) = 1 - a_L \exp[-\hat{x}^2/L_\beta^2] - a_R \exp[-(1-\hat{x})^2/L_\beta^2]$ with $\hat{x} = x/L_x$. The parameters a_L and a_R are set to 1 for boundary gradient driven cases (as described above), or can be respectively set to 0 if source and/or sink terms $\hat{\Lambda}_Q(x)$, or a free outflow condition on the outer boundary, are activated.

The vorticity around the radial boundaries can be approximately set to zero, when equivalently the right hand side $\hat{\sigma} = \hat{N}_e(\mathbf{x}) - Z_i\Gamma_{1i}\hat{N}_i(\mathbf{x})$ of the polarization equation, corresponding to the first order polarization density with FLR effects, is set to zero.

For this purpose it is most convenient to first define the boundary values of the gyroaveraged ion gyrocenter density $\hat{N}_{Gi}$ and then compute the consistent electron and ion gyrocenter densities in each time step (#3 in the algorithm), by re-setting $\hat{N}_{Gi}(x,y) = \Gamma_{1i}\hat{N}_i(x,y) \to [\hat{N}_{Gi}(x,y) - \hat{N}_0(x)] \cdot \beta(\hat{x}) + \hat{N}_0(x)$. This leaves the bulk density unchanged and gives a smooth radial transition to the initial profile values $\hat{N}_0(x)$ only in narrow regions of width L_β. The corrected ion gyrocenter density is then computed by $\hat{N}_i = \Gamma_{1i}^{-1}\hat{N}_{Gi}$ in $\mathbf{k}$ space and re-set in the boundary region. The electron density is re-set to $\hat{N}_e \to [\hat{N}_e - \hat{N}_{Gi}] \cdot \beta(\hat{x}) + \hat{N}_e$, which ensures zero $\hat{\sigma}$ in the boundary region. A further correction could be applied to alternatively ensure zero E-cross-B vorticity $\hat{\Omega} = \hat{\boldsymbol{\nabla}}_\perp^2 \hat{\phi}$ at the boundaries, but tests have shown no significant changes or advantages, as the E-cross-B vorticity is reduced already jointly with the generalized vorticity at the boundaries in this approach. (In the delta-f limit both cases are identical.)

This condition $\hat{\sigma}|_{b.c.} \equiv 0$ avoids strong vorticity gradients at the x boundaries (and by this possibly related numerical instabilities), and in addition ensures well-defined solution of the polarization equation (see Appendix).

Existence of a unique solution to the generalized Poisson problem $\boldsymbol{\nabla} \cdot \mathbf{P} = \boldsymbol{\nabla} \cdot \varepsilon \boldsymbol{\nabla} \phi = \sigma$ requires fulfillment of a compatibility boundary condition. Taking the domain integral over the (x,y) area S, one has $\int_S d\mathbf{x}\ \boldsymbol{\nabla} \cdot \mathbf{P} = \int_S d\mathbf{x}\ \sigma$, and therefore $\int_{\delta S} dl\ \mathbf{P} \cdot \mathbf{n}_S = \int_S d\mathbf{x}\ \sigma$. This is ensured by the above vorticity-free and flow-free ($\mathbf{n}_S \cdot \boldsymbol{\nabla}\phi = \partial_x \phi = u_y \equiv 0$) conditions on the boundary δS in x (and periodicity in y). The condition correponds to global conservation of the polarization charge density.

D. Mirror padding for Fourier transforms

The algorithm involves four evaluations of gyro-operators (in steps #2, 3, 4, 6), which is in the present isothermal model achieved with high accuracy in **k** space by applying (FFTW3 library) Fourier transforms. Actually the evaluation of $\hat{N}_i = \Gamma_{1i}^{-1}\hat{N}_{Gi} = [1-(1/2)\tau_i\boldsymbol{\nabla}^2]\hat{N}_{Gi}$ in Padé approximation for the vorticity free boundary condition (step #3) could alternatively be achieved by (considerably faster but less accurate) finite differencing in **x** space. Although more costly, this evaluation is here for consistency also done in **k** space.

Standard Fourier transformation requires periodic boundary conditions, else discontinuities would introduce Gibbs noise artefacts. The radial "physical" domain $0 \leq \hat{x} \leq 1$ however usually includes density profiles with $\hat{N}_s(\hat{x}=0) \neq \hat{N}_s(\hat{x}=1)$. For this reason, ghost domains in an extended $\hat{x}$ direction are introduced for the (x, y) field arrays before solution by Fourier transforms to **k** space, and also before solution of the polarization equation.

Doubling the (initially "quarter-wave" physical) domain to $0 \leq \hat{x} \leq 2$, by copying the initial array $f(\hat{x}, \hat{y})$ into the region $1 < \hat{x} \leq 2$ and defining symmetrically mirrored $f(\hat{x}) \equiv \hat{f}(1-\hat{x})$ for $0 \leq \hat{x} \leq 1$ ensures ("half wave") $\hat{x}$ periodicity of field functions. Full-wave input functions to the gyro-averaging Fourier transforms are achieved by a further anti-symmetric domain doubling with boundary offset correction: the four-fold extended array includes $f(4-\hat{x}) = 2f(0) - f(\hat{x})$ for $2 < \hat{x} \leq 4$. This ensures full-wave radial representation of the densities in the gyro-averaging Fourier transforms, but for a four-fold computational cost.

It is as usual favourable to use power-of-two numbers of grid points in the $\hat{x}$ and $\hat{y}$ directions, so that the FFTW3 library will make use of Fast Fourier Transform (FFT) algorithms. Any other grid size can be chosen, but FFTW3 then automatically uses somewhat (depending on the grid size) slower Discrete Fourier Transform (DFT) methods.

V. PARALLELIZATION AND REPRODUCIBILITY

The present development and production run platforms for the TIFF code are multi-core shared memory office workstations, so that multi-core and/or multi-thread parallelization is simply achieved by OpenMP (OMP) parallelization of grid array sized double loops, and use of the respective OMP library of FFTW3 for the Fourier transforms. The frequent transistions between single and parallel regions, required by the above algorithm, prevent

good scaling. Efficient speed-up is usually achieved (depending on the input parameters and on the hardware) when between 8 and 32 parallel threads are used.

Bitwise reproducibility of subsequent executions on the same system can be achieved when the "ESTIMATE" flag for the transform planner routine of the FFTW3 library is used, which is desirable for verification and testing purposes. The "MEASURE" flag is faster in execution (which would be desirable for long production runs with for example millions of time steps) but not regularly bitwise reproducible [65], because it might choose different algorithms depending on the system background load, which can be quickly noticeable in the turbulent phase of simulations due to the highly nonlinear nature of the present set of equations. This may not be relevant if anyhow only statistical diagnostic quantities of a saturated fully turbulent state are of interested.

The TIFF code presently uses only the FFTW and OMP libraries and can be compiled for example with the GNU gcc compiler, which are all available as standard in most usual Linux distributions. This ensures usability on most consumer PCs or workstations.

VI. DIAGNOSTIC OUTPUT

Diagnostic outputs are produced only every n_D-th time steps. For n_D large (in the order of hundreds or thousands of time steps) this allows real-time diagnostics with little post-processing, which greatly reduces the necessary output storage space (in comparison to writing all arrays for each computational time step).

The 2d dynamical field arrays $\hat{N}_e(i,j)$, $\hat{N}_i(i,j)$, $\hat{\phi}(i,j)$, $\hat{\omega}(i,j)$, $\hat{\sigma}(i,j)$, and $\tilde{N}_e(i,j) = \hat{N}_e(i,j) - \hat{N}_0(i)$ are regularly written out (e.g. to a RAM disc), and can be viewed (already during run time) with any 2d visualization software (for which presently a simple gnuplot script is used). In addition, 1d cross sections of several arrays $f(i,j_0)$ and $f(i_0,j)$, and averaged radial profiles $\langle f \rangle_j(i)$ are written.

Spectra $\langle f(k_x) \rangle_j$ and $\langle f(k_y) \rangle_i$ are computed at each diagnostic output step for several quantities, such as kinetic energy, enstrophy, and density and potential power spectra.

Energetic and transport quantities are recorded as time traces of (x,y) domain averages. The (normalized) E-cross-B advective electron particle transport is obtained as $Q_n(t) = (1/S) \int d\mathbf{x}\ \hat{N}_e(x,y) \partial_y \hat{\phi}(x,y)$, where $S = L_x L y$, and the y derivative is provided by simple centered finite differencing (as also in the following diagnostics).

The full-f global thermal free energy is given by (compare ref. [59]): $E_T = E_{Te} + \tau_i E_{Ti}$ with $E_{Ts} = (1/S)\int d\mathbf{x}\ [\hat{N}_s(\ln \hat{N}_s - \ln \hat{N}_0) - (\hat{N}_s - N_0)]$. The kinetic energy is $E_K = (1/2S)\int d\mathbf{x}\ \hat{N}_i(\hat{\boldsymbol{\nabla}}\hat{\phi}_G)^2$. The total energy is an ideal conserved quantity, and can be used as a diagnostic for saturation of a turbulent state.

Further diagnostics can be included, for example output and computation of difference norms for solver testing against a constructed solution, or center-of-mass calculation of an interchange driven "blob".

VII. DELTA-F LIMIT

The TIFF code also implements the corresponding 2d isothermal delta-f set of gyrofluid equations concurrent to the full-f model. Where possible both use the same procedures, or enter forks for specific treatment. This allows cross-verification of the full-f model in its small-amplitude limit with the original delta-f model within the same code and for equal methods and (initial and boundary) conditions.

The equivalently normalized delta-f set of equations is:

$$\hat{\partial}_t \hat{N}_e + \{\hat{\phi}, \hat{N}_e\} = \lambda_c \hat{\Lambda}_c + \lambda_B \hat{\Lambda}_{Be} + \lambda_S \hat{\Lambda}_{Se} \tag{16}$$

$$\hat{\partial}_t \hat{N}_i + \{\hat{\phi}_i, \hat{N}_i\} = \lambda_B \hat{\Lambda}_{Bi} + \lambda_S \hat{\Lambda}_{Si} \tag{17}$$

$$\frac{1}{\tau_i}(\Gamma_{0i} - 1)\,\hat{\phi} = \hat{\sigma} \tag{18}$$

The (modified) delta-f HW term is $\hat{\Lambda}_{ce} = \hat{\alpha}[(\hat{\phi} - \langle\hat{\phi}\rangle) - (\hat{N}_e - \langle\hat{N}_e\rangle)]$. Sheath coupling is described by $\hat{\Lambda}_{Se} = \gamma_D[(1 + \Lambda_D)\tilde{N}_e - \hat{\phi}]$ and $\hat{\Lambda}_{Si} = \gamma_D \tilde{N}_e$. The curvature terms are $\hat{\Lambda}_{Bs} = \mathcal{K}(\hat{\phi}_s) + \tau_s \mathcal{K}(\hat{N}_s)$. Hyperviscosity equivalently now acts on $\hat{N}_s$.

In $\hat{\sigma} = \hat{N}_e(\mathbf{x}) - Z_i \Gamma_{1i} \hat{N}_i(\mathbf{x})$ the gyrocenter densities $\hat{N}_s = \tilde{N}_s/N_0$ here denote the fluctuating components only. Equivalently to the full-f version, the radial density profile is also included into the initialization of the densities and evolved accordingly, and is not decoupled by a gradient parameter, so that the same (not periodic) boundary conditions on the x domain apply as for the full-f case described above. This leads to additional boundary damping in contrast to doubly periodic (physical) domains, so that the results can only be qualitatively compared with usual fluid HW code results.

The solution algorithm is basically the same as for the full-f model described above. Steps # 4-6 are reduced to evaluating the delta-f (full-k) polarization eq. (18) in k space with the

Padé approximation of Γ_{0i} through $\hat{\phi}_k = -[\hat{k}^2/(1+\tau_i\hat{k}^2)]\ \hat{\sigma}_k$. The long-wavelength (low-k) form of this delta-f polarization is optionally obtained by setting the term $\tau_i\hat{k}^2 \equiv 0$ herein. The gyrofluid ion potential (step #7) is simply $\hat{\phi}_i = \Gamma_{1i}\hat{\phi}$.

For diagnostics, the delta-f total thermal free energy is evaluated as $E_T = (1/S)\int d\mathbf{x}[(\hat{N}_e - \hat{N}_0)^2 + \tau_i(\hat{N}_i - \hat{N}_0)^2]$ and kinetic energy as $E_K = (1/2S)\int d\mathbf{x}\ (\hat{\boldsymbol{\nabla}}\hat{\phi}_i)^2$, while the transport and other output quantities remain the same as for the full-f model.

VIII. TEST OF GENERALIZED POISSON SOLVERS

In step # 5 of the full-f TIFF algorithm, the polarization equation in the form of a generalized 2d Poisson problem $\boldsymbol{\nabla}\cdot\varepsilon\boldsymbol{\nabla}\phi = \sigma$ has to be solved for the unknown ϕ. Equivalent problems arise in other physical scenarios, such as for spatially variable dielectric with permittivity $\varepsilon(\mathbf{x})$ and a given (negative) space charge distribution $\sigma(\mathbf{x})$. Iterative solution algorithms are routinely applied on such problems, but in most applications the inhomogeneity in ε is usually small, whereas it can vary strongly in our case of a turbulent edge plasma. Iterative solvers may converge slowly in such situations, if at all.

The present TIFF code implementation includes a choice between an iterative preconditioned conjugate gradient (PCG) solver, an iterative red-black successive over-relaxation (SOR) solver, and a novel "dynamically corrected" Fourier (DCF) solver. The solution algorithms are described in detail in the appendix. Other solvers are of course possible, perhaps faster, and may be further implemented and tested in future. The full-f gyrofluid FELTOR code for example also includes a discontinuous Galerkin method or a multi-grid scheme, in addition to a (different) conjugate gradient scheme [39].

Here the PCG, SOR and DCF solvers in TIFF are compared by method of a constructed solution as a component test, and within the full code setup by cross-verification with recent "blob" dynamics results from the FELTOR code. The main aspect here lies on (cross) verification and determination of accuracy of the new DCF scheme, which is suggested as a stable and (predictably) efficient solution method for application on the generalized Poisson problem of the full-f polarization equation, that is applied in each (small) time step of a dynamically evolving turbulence code.

The dynamical context is important, because the underlying "Teague method", introduced in different context, for approximate solution of a generalized Poisson-type problem,

is in itself not very accurate. Here however an efficient dynamical (or recursive) correction based on the solution from the previous time step is newly applied with the "Teague method", which is shown to improve its accuray by two orders of magnitude, and by that can achieve similar accuracy as iterative solvers with a "reasonable" (affordable) number of iterations in a turbulence code.

A. Teague's original method

In optics, the "transport of intensity equation" (TIE) is an approximate relation for the intensity and the wave phase of a coherent beam in an optical field [69, 70]. The underlying mathematical form of the TIE is basically equivalent to the 2d generalized Poisson problem: $\boldsymbol{\nabla} \cdot I(\mathbf{x}) \boldsymbol{\nabla} \psi(\mathbf{x}) = -k \partial_z I(\mathbf{x})$, where I is the known (measured) planar intensity distribution at a distance z, k the wave number, and ψ the sought phase of the wave. Various solution methods have been used on the TIE in the field of applied optics [70], but a now widely used approximate Fourier method has been suggested by Teague in 1983 [69] by introducing what is now commonly known as Teague's auxiliary function.

In the following this original "Teague's method" is described in terms of the notation introduced in the previous sections in context of the gyrofluid polarization equation (and not in the TIE notations used in optics). Starting with

$$\boldsymbol{\nabla} \cdot [\varepsilon(\mathbf{x}) \boldsymbol{\nabla} \phi(\mathbf{x})] = \sigma(\mathbf{x}), \tag{19}$$

an auxiliary 2d scalar function $p(\mathbf{x})$ is introduced that is supposed to satisfy

$$\varepsilon(\mathbf{x}) \boldsymbol{\nabla} \phi(\mathbf{x}) \equiv \boldsymbol{\nabla} p(\mathbf{x}). \tag{20}$$

This reduces the generalized Poisson problem to an ordinary 2d Poisson equation

$$\boldsymbol{\nabla}^2 p(\mathbf{x}) = \sigma(\mathbf{x}) \tag{21}$$

which can, for example, be efficiently inverted and solved by Fourier transformation into $\mathbf{k}$ space (and back-transformation of the solution) as $p(\mathbf{k}) = -(1/k^2)\sigma(\mathbf{k})$, or by any other fast Poisson solver. The defining auxiliary relation eq. (20) can be re-written as $\boldsymbol{\nabla} \phi(\mathbf{x}) = [\boldsymbol{\nabla} p(\mathbf{x})]/\varepsilon(\mathbf{x})$, on which the divergence operator is applied on both sides to obtain:

$$\boldsymbol{\nabla}^2 \phi(\mathbf{x}) = \boldsymbol{\nabla} \cdot \frac{1}{\varepsilon(\mathbf{x})} \boldsymbol{\nabla} p(\mathbf{x}). \tag{22}$$

The right hand side contains the (by now) known quantities $\varepsilon(\mathbf{x})$ and $p(\mathbf{x})$, and can be evaluated by standard fourth order 2d centered finite differencing in x and y. Eq. (22) can therefore again be solved (e.g. in $\mathbf{k}$ space) to obtain $\phi(\mathbf{x})$. When Fourier transforms are used, the method involves four evaluations (two forward and two backward) of the 2d transform $\mathcal{F}$, which can be formally expressed (compare ref. [71] for the TIE version) as:

$$\phi(\mathbf{x}) = \mathcal{F}^{-1}\left[-\frac{1}{k^2}\mathcal{F}\ \boldsymbol{\nabla}\cdot\frac{1}{\varepsilon}\boldsymbol{\nabla}\mathcal{F}^{-1}\left(-\frac{1}{k^2}\mathcal{F}\sigma\right)\right]. \tag{23}$$

Apparently the accuracy of Teague's method is considered mostly sufficient for solution of the TIE in optics, as it is widely applied. However, it has of course been noted that the introduction of the auxiliary function p in eq. (20) is in general mathematically incomplete, and this approximation may introduce an unspecified error into the solution [72, 73]. The definition of eq. (20) would actually hold exactly for a truly conservative nature of the vector field $\mathbf{P}(\mathbf{x}) \equiv \varepsilon(\mathbf{x})\boldsymbol{\nabla}\phi(\mathbf{x})$, but this condition of irrotationalty is in general not ensured, neither in the TIE of optics, nor in polarization of electrostatics.

Rather, the complete Helmholtz decomposition of the vector field $\mathbf{P}(\mathbf{x})$ is:

$$\mathbf{P} = \varepsilon\boldsymbol{\nabla}\phi \equiv \boldsymbol{\nabla}p + \boldsymbol{\nabla}\times\mathbf{H} \tag{24}$$

with a scalar potential $p(\mathbf{x})$ and a vector potential $\mathbf{H}(\mathbf{x})$. This general form provides the same solution path for $p(\mathbf{x})$ like above, as still $\boldsymbol{\nabla}\cdot\mathbf{P} = \boldsymbol{\nabla}^2 p = \sigma$ holds. The next step, generalizing the result of eq. (22), now gives:

$$\begin{aligned}\boldsymbol{\nabla}^2\phi(\mathbf{x}) \ &= \ \boldsymbol{\nabla}\cdot\frac{1}{\varepsilon(\mathbf{x})}\boldsymbol{\nabla}p(\mathbf{x}) \ + \ \boldsymbol{\nabla}\cdot\frac{1}{\varepsilon(\mathbf{x})}\boldsymbol{\nabla}\times\mathbf{H}(\mathbf{x}) \\ &= \ \boldsymbol{\nabla}\cdot\frac{1}{\varepsilon(\mathbf{x})}\boldsymbol{\nabla}p(\mathbf{x}) \ + \ \left\{\frac{1}{\varepsilon},\eta\right\}\end{aligned} \tag{25}$$

with $\boldsymbol{\nabla}\cdot(1/\varepsilon)\boldsymbol{\nabla}\times\mathbf{H} = (\boldsymbol{\nabla}\times\mathbf{H})\cdot\boldsymbol{\nabla}(1/\varepsilon) = \{(1/\varepsilon),\eta\}$, where the 2d Poisson bracket notation (defined above) is used, and η is the z component of (unknown) $\mathbf{H}(x,y) = \eta(x,y)\ \mathbf{e}_z$.

To find a constraint on η, one can apply the curl operator on both sides, instead of the divergence operator $\boldsymbol{\nabla}\cdot\boldsymbol{\nabla}\phi = \boldsymbol{\nabla}\cdot...$, correspondingly as in eq. (25). This gives the condition $\boldsymbol{\nabla}\times\boldsymbol{\nabla}\phi = \boldsymbol{\nabla}\times(1/\varepsilon)\boldsymbol{\nabla}p + \boldsymbol{\nabla}\times[(1/\varepsilon)\boldsymbol{\nabla}\times\mathbf{H}] = 0$, resulting in:

$$\boldsymbol{\nabla}\cdot\left(\frac{1}{\varepsilon}\boldsymbol{\nabla}\eta\right) = \left\{\frac{1}{\varepsilon},p\right\}. \tag{26}$$

This determining relation for the unknown η however again has the form of a generalized Poisson equation, which sends us back to start...

Another constraint can be generated by taking the curl on $\mathbf{P}$, which gives the relation $\boldsymbol{\nabla} \times (\varepsilon \boldsymbol{\nabla} \phi) = \boldsymbol{\nabla} \times \boldsymbol{\nabla} \times \mathbf{H}$. This can be rephrased as:

$$\boldsymbol{\nabla}^2 \eta = \{\phi, \varepsilon\}. \tag{27}$$

This first shows that a sufficient condition for the accuracy of Teague's method would be that $\{\phi, \varepsilon\} = \boldsymbol{\nabla}\phi \times \boldsymbol{\nabla}\varepsilon \equiv 0$, which holds if the isocontours of ϕ and ε were aligned everywhere [72]. The relation can also be used to derive constraints for the error norm [72].

If applied to gyrofluid simulations, the error is surely not negligible as $\{\phi, \varepsilon\} \sim \{\phi, N_i\}$ for constant magnetic field, and thus directly related to the advective ion nonlinearity.

B. Iterative and dynamical corrections

Iterative methods have been suggested to correct the error by the original Teague approximation. In ref. [74] a Picard-type iteration is applied, that uses an initial solution ϕ_0 by Teague's method (without need to refer to the vector potential) to compute an according source term $\sigma_0 \equiv \boldsymbol{\nabla} \cdot \varepsilon \boldsymbol{\nabla} \phi_0$, then use $\Delta\sigma = \sigma_0 - \sigma$ in another turn of application of Teague's method to obtain a correction $\Delta\phi$, and repeat until $\Delta\phi$ is smaller than a specified error.

The set of equations (25) and (27) allows a further possibilities of an iterative approach. A first approximation for $\phi^{(0)}$ is obtained by setting $\eta^{(0)} = 0$ in eq. (25), which corresponds to the original Teage approximation; then compute an approximate $\eta^{(1)}$ from exact solution of eq. (27) using this approximate $\phi^{(0)}$, and with that obtain an updated $\phi^{(1)}$ from solution of eq. (25); and iterate further until a desired error bound is reached.

In the following, this recursive correction (here denoted as "RCF method") based on eqs. (25) and (27) will be tested by means of a constructed solution. However, any such iterative methods involve multiple evaluations of Fourier transforms (or other fast conventional Poisson solvers) per iteration step, and can become expensive when the iterative evaluation has to be carried out in every of very many time steps in a dynamical turbulence simulation.

It will be shown that already after one or two iterations a high accuracy is reached. This motivates another possible non-iterative correction to Teague's method in the context of a dynamical simulation with time evolution of $\phi(t)$ in the presence of small time steps. In simulations of fully developed turbulence, and in particular when an explicit finite difference scheme is used like in the present code, the time step Δt, as it appears in eq. (15), is small,

and so accordingly is the difference between successive solutions $\phi^{(t)}$ and $\phi^{(t-1)}$.

The idea is to therefore evaluate

$$\eta_o(\mathbf{x}) \equiv \boldsymbol{\nabla}^{-2}\{\phi^{old}, \varepsilon\} \tag{28}$$

with an "old" solution from previous time steps in a dynamical simulation, and with this approximation compute

$$\phi(\mathbf{x}) = \boldsymbol{\nabla}^{-2}\left[\boldsymbol{\nabla}\cdot\frac{1}{\varepsilon}\boldsymbol{\nabla}\left(\boldsymbol{\nabla}^{-2}\sigma\right) + \left\{\frac{1}{\varepsilon}, \eta_o\right\}\right]. \tag{29}$$

In contrast to iterative schemes applied within each time step, this reduces the additional expense for the correction to only one (for example FFT based) inversion of the conventional Poisson problem, and (comparatively cheap) computation of another Poisson bracket. In the very first time step one can simply use $\eta_o = 0$ and thus obtain an uncorrected approximate solution for ϕ by the conventional Teague method. It is feasible to simply use $\phi^{old} \equiv \phi^{(t-1)}$ of the previous time step. In the present code an extrapolation is applied as:

$$\phi^{old} \equiv \phi^{(t-1)} + a\cdot(\phi^{(t-1)} - \phi^{(t-2)}) \tag{30}$$

with a free estimator factor $a \in (0, 1)$. Because this extension of Teague's method uses previous results of a time evolving simulation, and evaluates the multiple occuring inversions of the Poisson problem with Fourier solvers in $\mathbf{k}$ space, it is in the following abbreviated as the "DCF" (dynamically corrected Fourier) method. The accuracy however will here depend on the size of the (small) dynamical time step.

C. Unit test of generalized Poisson solvers

The specific implementation of the PCG, SOR and DCF solvers as used in the TIFF code is in detail described in the Appendix. The code can be run with a unit testing option, by setting a flag in the input parameter file, that initialises analytical constructed functions ε_c and σ_c and only calls the specified Poisson solver once, so that the numerical solutions for ϕ can be directly compared with the analytical function ϕ_c. The main purpose of this test is to determine the applicability and accuracy of the novel dynamically corrected Fourier (DCF) solver in comparison to the established SOR and PCG methods.

As constructed solutions, here $\phi_c \equiv \phi_{c0}\sin(xk_x)\sin(yk_y)$ and $\varepsilon_c \equiv 1 - gx + a\sin(xk_n)\sin(yk_n)$ are exemplarily specified, and the corresponding $\sigma_c = \boldsymbol{\nabla}\cdot\varepsilon_c\boldsymbol{\nabla}\phi_c =$

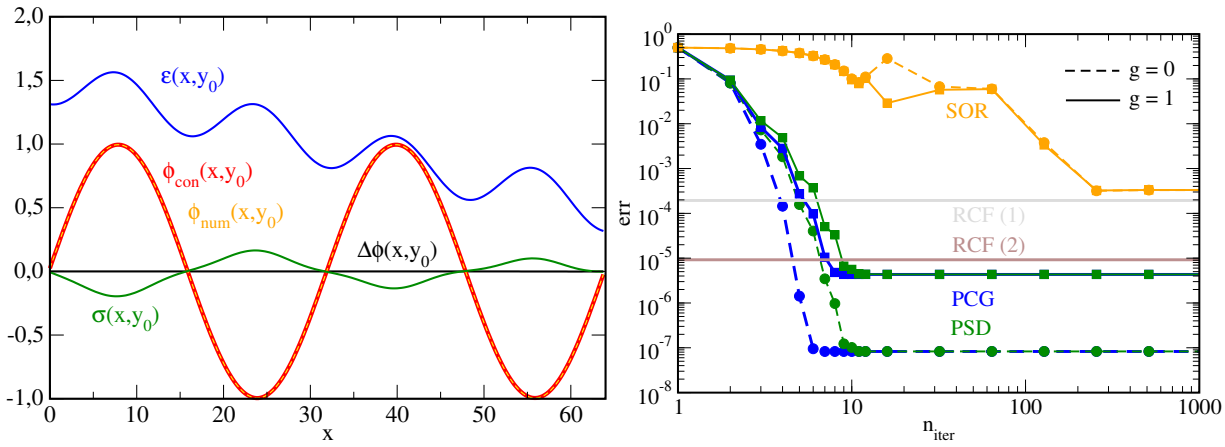


FIG. 2: Left: Constructed solution ϕ_c (red) and ε_c (blue) and corresponding $\sigma_c = \boldsymbol{\nabla} \cdot \varepsilon_c \boldsymbol{\nabla} \phi_c$ (green), shown as a function of x at $y_0 = (L_y/2 - 5)$. The difference $\Delta\phi$ (black) from the numerical solution (dashed orange) obtained with the RCF(1) method for $N_x = N_y = 256$ is here too small to be visible. Right: Global L_2 error norm obtained from different solvers (see main text) after n_{iter} iterations with ($g = 1$, solid) and without ($g = 0$, dashed) a background gradient in ε_c.

$\varepsilon_c(\partial_x^2\phi_c + \partial_y^2\phi_c) + (\partial_x\varepsilon_c)(\partial_x\phi_c) + (\partial_y\varepsilon_c)(\partial_y\phi_c)$ is also given analytically. In the following test, $\phi_{c0} = 1$, $a = 0.2$, $g = 0$ or 1, $k_x = 2(2\pi/L_X)$, $k_y = 3(2\pi/L_y)$ and $k_n = 4(2\pi/L_x)$ are set.

The constructed and numerical solutions are shown in Fig. 2 (left) as a function of x at $y_0 = (L_y/2 - 5)$. The differences $\Delta\phi(x, y)$ between constructed and numerical solutions can be visualised and compared by their global L_2 norms as a function of resolution or iterations.

In Fig. 2 (right) the global error $err = ||\Delta\phi||_2$ is generally large for $g = 1$ when a background gradient in $\varepsilon_c(x)$ (solid lines) is present and discontinuities in the derivatives occur at the x boundaries. For comparison, also results for the above constructed solution but with $g = 0$ (constant background, periodic $\varepsilon_c(x)$, dashed lines) is shown, with reduced more "ideal" errors. In practice, the $g = 0$ case would for example correspond to a "seeded blob" simulation scenario, whereas the $g = 1$ case would be relevant to gradient driven drift wave turbulence scenarios.

The error err is shown as a function of the number of iterations n_{iter} for different solvers, on a square equidistant grid with $N = N_x = N_y = 256$. For reference the two horizontal bold lines denote the error for $g = 1$ of the recursively corrected Fourier (RCF) method after one recursion (grey line) and after two recursions (brown line). The dynamically corrected

Fourier solver (DCF) uses recursion by means of the value ϕ_0 from the last dynamical time step and therefore can not be quantified with a unit test, but one might expect an error of the DCF solver in between the RCF(1) and RCF(2) solvers. For higher recursion numbers (≥ 4) the error of the RCF solver approaches the error of the high n_{iter} limits of the PCG (blue, solid line) and PSD (green, solid line) solvers, as all of those schemes employ Fourier methods and fourth order finite differencing. (The pre-conditioned steepest descent (PSD) solver is described in the Appendix in context of the PCG solver.) The error (for $g = 1$) of the PCG scheme is after $n_{iter} = 5$ iterations comparable to the RCF(1) scheme. The computing times of RCF and PCG are here for this PCG iteration number also similar.

The following table depicts the L_2 error and order for the $g = 0$ test case above, given with the RCF(4) scheme with four recursive iterations as a function of grid resolution $h \sim N_0/N$. The order is calculated as $O = \log(||\Delta\phi||_2^{(h)}/||\Delta\phi||_2^{(h/2)})/\log(2/1)$. A higher number of iterations does not give further improvement in this case. The table shows the expected scaling with fourth order accuray, which corresponds to the order of the finite difference schemes used in the evaluation of the right hand side terms in eq. (25).

N	err	O
16	$1.808 \cdot 10^{-2}$	-
32	$1.251 \cdot 10^{-3}$	3.85
64	$7.998 \cdot 10^{-5}$	3.96
128	$5.036 \cdot 10^{-6}$	3.99
256	$3.154 \cdot 10^{-7}$	4.00
512	$1.972 \cdot 10^{-8}$	4.00
1024	$1.226 \cdot 10^{-9}$	4.01
2048	$7.113 \cdot 10^{-11}$	4.11

TABLE I: L_2 norm error and order of accuracy for various square grid point numbers $N = N_x = N_y$ for the constructed solution test case (compare Fig. 2), obtained with the "recursively corrected Fourier" (RCF) method after 4 iterations.

The second order accurate SOR scheme (orange lines in Fig. 2) has much slower convergence and does for this resolution never reach the accuracy of the (fourth order) RCF and PCG schemes. Usually several hundred SOR iterations are required for acceptable results

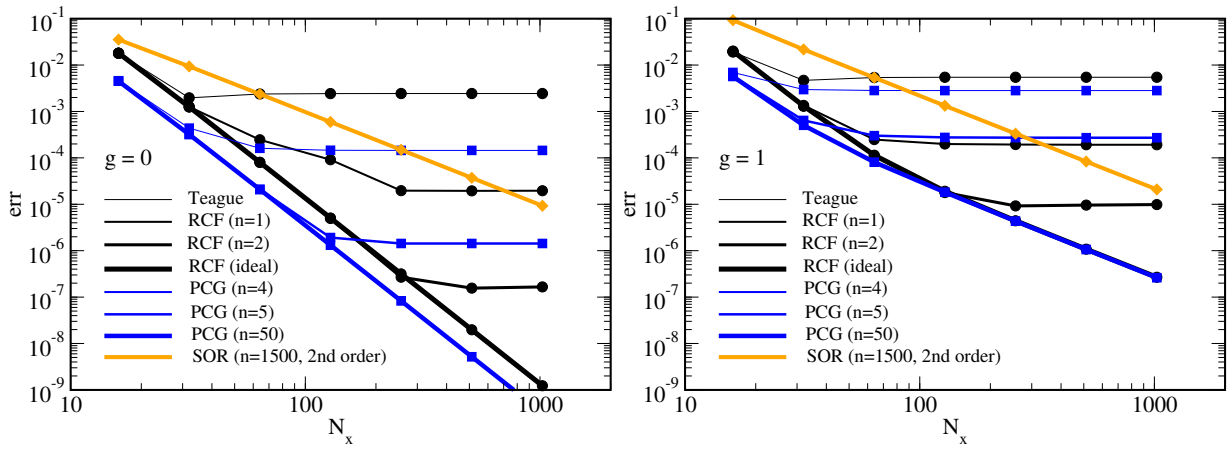


FIG. 3: L_2 error norm, related to the constructed solution as a function of number of grid points $N_x = N_y$, for various generalized Poisson solvers (see main text). As expected, for $g = 0$ (left figure, periodic functions) the RCF and PCG solvers show a fourth order dependence (for large iteration numbers n), and the SOR solver a second order dependence. For $g = 1$ (right figure, nonperiodic ε_c with background gradient) the errors are larger for all solvers due to boundary discontinuity in the x derivatives.

in the unit test, where the initial $\phi(n_{iter} = 0) \equiv 0$ for the iteration is zero. The convergence (for a given error tolerance) however improves drastically within a dynamical simulation, when the initial $\phi(n_{iter} = 0)$ of the iteration is projected from the result $\phi(t - 1)$ of the previous time step.

In Fig. 3 the error is shown as a function of the resolution in terms of the number of grid points $N_x = N_y$, with otherwise same parameters as above. The case of periodic density ($g = 0$) is shown in the left figure: for a large number of iterations ($n_{iter} = 50$) the PCG scheme (bold blue line) follows the expected fourth order dependence on resolution, whereas the SOR scheme (bold orange line, $n_{iter} = 1500$) shows the second order dependence $err \sim N_x^{-2}$ (i.e., a slope of -2 in the log-log plot). The "ideal" RCF scheme (bold black line) here denotes a correction term calculated once from the constructed solution ϕ_c instead of recursively, which also shows a fourth order (N_x^{-4}) slope, as expected.

The gradually thicker black lines (from top to bottom) show, topmost, the error of the original "Teague method" without correction, which is for usual resolutions always in the range of $2 \cdot 10^{-3}$ for $g = 0$ (left figure). The RCF(1) scheme uses one recursion of the solver in the unit test problem, and already gives an improvement of the error by around two orders

of magnitude. The RCF(2) scheme with two recursions follows the "ideal" dependence until around $N_x = 256$ and for higher resolution saturates at an error of around $2 \cdot 10^{-7}$. The gradually thicker blue lines (from top to bottom) show the error by the PCG scheme after 4, 5 and 50 iterations. The $n_{iter} = 5$ case for PCG has for high resolution an error in between the results from the RCF(1) and RCF(2) schemes.

The right Fig. 3 shows the corresponding results for $g = 1$ in the presence of a background gradient, which in the present implementation of the solvers in TIFF overall reduces the achievable accuracy. The general behaviour of the different solvers is similar to the $g = 0$ results, but no "ideal" scaling of the error (-4 power law) with resolution is obtained any more. The RCF(1) and PCG(4) schemes also show similar errors for medium to large resolution.

The dynamically corrected Fourier (DCF) scheme needs three evaluations of the standard Poisson problem, which is here presently achieved by a fast Fourier solver. In a dynamical simulation the error correction then is calculated from the previous time step solution. The PCG scheme needs one evaluation of a standard Poisson inversion (e.g. by Fourier solver) per iteration step, so that PCG ($n = 3 - 4$) has approximately the same computational cost as a DCF evaluation (which in addition needs another call of a Poisson bracket evaluation). The necessary number of iterations in PCG or SOR to reach a given accuracy can strongly depend on the complexity of the problem, basically determined by the degree of variability of $\varepsilon(x, y, t)$. The computational expense of the DCF method only depends on the size of the grid. The DCF scheme therefore presents itself as a viable alternative method (for moderate accuray) with predictable run times.

D. Cross-verification of full-f full-k blob simulation

The unit testing of the PCG, DCF and SOR solvers above has been applied on the "pure" generalized Poisson equation $\boldsymbol{\nabla} \cdot \varepsilon \boldsymbol{\nabla} \phi = \sigma$. The implementation in the TIFF code for solution of the full-f full-k gyrofluid polarization eq. (9) requires for $\tau_i \neq 0$ two additional applications of (here Fourier based) solvers for the $\sqrt{\Gamma_0}$ operator, and further (also Fourier based) evaluations of the gyro-averaging operator $\Gamma_1 N_i$ in σ, and of $\Gamma_1 \phi$ in the ion gyrocenter density advection.

As a further test, an overall cross-verification of the code is intended by running a seeded

"blob" simulation for parameters that correspond to a recent study with the full-f full-k gyrofluid isothermal version of the FELTOR code, described by Held and Wiesenberger in ref. [59] and shown in Figures 4-7 therein.

The simulation plasma input parameters for this case are: ion to electron temperature ratio $\tau_i = 4$, magnetic curvature $\kappa = 1.5 \cdot 10^{-4}$, normalization scale $\delta = 1$, non-adiabaticity $\hat{\alpha} = 0$, and absence of a sheath ($\hat{\Lambda}_{Ss} = 0$). The square domain is $L_x = L_y = 200\rho_s$ with resolution $N_X = N_y = 1024$. The initial perturbation is a Gaussian "blob" in electron density of width $w = 5\rho_s$ and peak amplitude $\Delta\hat{N} = 1$ centered at $x_0 = 25$ and $y_0 = 100$, on a constant background with $\hat{N}_0 = 1$. The initial perturbed ion gyrocenter density is either set equal to the electron density (which introduces an initial blob spin), or for a "vorticity free" initialization to $\hat{N}_i = \Gamma^{-1} N_e$. The x boundary density values are pinned in a small zone $L_\beta = 2\rho_s$. The hyperviscosity is set to $\nu_4 = 10^{-5}$, and in accordance to ref. [59] an additional physical viscosity $\nu_2 = 3 \cdot 10^{-5}$ is applied. The time step is set to $\Delta\hat{t} = 0.1$ and run for $I_{max} = 23040$ steps with diagnostic outputs at every $I_{out} = 320$ steps. The iterative error bound for the PCG and SOR solvers was set to $err = 10^{-3}$ with 500 iterations maximum.

The ExB vorticity $\hat{\Omega}(x, y) = \hat{\boldsymbol{\nabla}}^2\hat{\phi}$ of the evolved blob at the final time $\hat{t} = 2304$ in units of ρ_s/c_s is compared in Fig. 4 for simulations with the different PCG, DCF and SOR solvers used for the polarization. For this plot the zero vorticity initial conditions is chosen. The blob gradually acquires gyro-induced FLR spinning and the propagation has characteristic up-down asymmetry.

The three solvers show visually very similar results regarding the fine structure and global quantities such as the center-of-mass position of the blob. For comparison the corresponding result obtained with the original Teague method (without correction) is shown in frame (d). Shape and position are similar but with clear differences in details. These plots can be compared with the result of FELTOR simulations of Figure 4 (bottom middle frame) in ref. [59]. Note that the FELTOR blob has initial position $x_0^{FELTOR} = 50$, whereas here it is at $x_0^{TIFF} = 25$. A blob front position of $x_F^{TIFF} \approx 125$ in our results thus corresponds to a position $x_F^{FELTOR} \approx 150$ in the referenced results and figure. The overall structure and position is similar, but fine details (e.g. the tilt of the blob head, and structures in the secondary trailing vortices) are clearly different between the TIFF and FELTOR codes, which employ different solvers for the Poisson problem and the gyro operators.

Fig. 5 shows basically the same set-up but with nonzero vorticity initialisation achieved

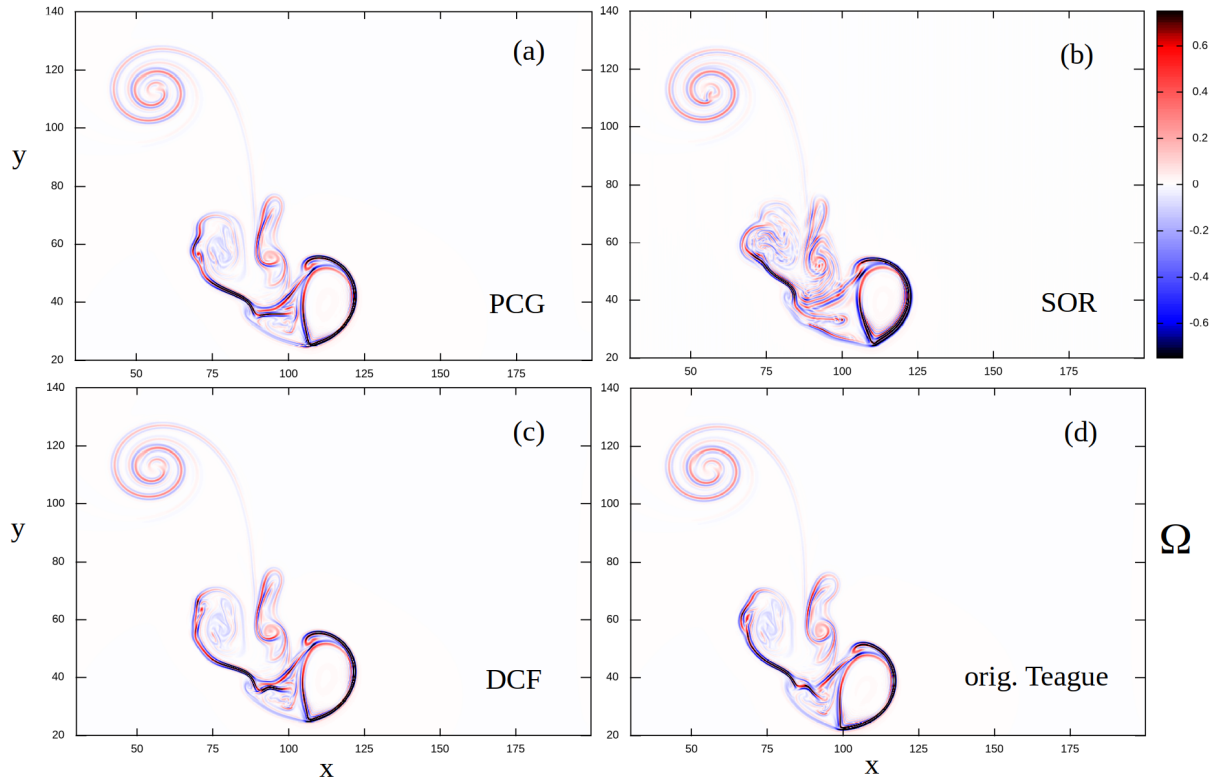


FIG. 4: Comparison of vorticity $\hat{\Omega} = \hat{\boldsymbol{\nabla}}^2\hat{\phi}(x,y)$ for an evolved seeded blob ($\tau_i = 4$, $\hat{N}_0 = 1$, $w = 5$) with zero vorticity initial condition ($\hat{N}_i = \Gamma^{-1}N_e$), at $\hat{t} = 2304$, for different generalized Poisson solvers. (a) PCG; (b) SOR; (c) DCF; (d) original (uncorrected) Teague solver.

by setting $\hat{N}_i = \hat{N}_e$. The initial spin largely compensates the later FLR spin build up, so that propagation has much straighter radial ("to the right") direction with less up-down asymmetry. Again the PCG, DCF and SOR solvers show very close agreement. Here the result obtained with the original (uncorrected) Teague method is clearly off and shows a pronounced downward drift. These plots can again be compared with the corresponding Figure 4 (bottom right) in ref. [59]. The overall structure is again similar, and details in the vortex trail again differ. The most noteable difference is in the blob front position, where $x_F^{TIFF} \approx 175$ in our present results would be expected to correspond in FELTOR to 200, which is already the position of the right boundary. The actual FELTOR blob front position in ref. [59] at the same time appears to be at $x_F^{FELTOR} \approx 190$ only. A probable explanation for this difference between the FELTOR and TIFF code results could be in the respective handling of the (in this particular case very close) boundary conditions. The resolutions also

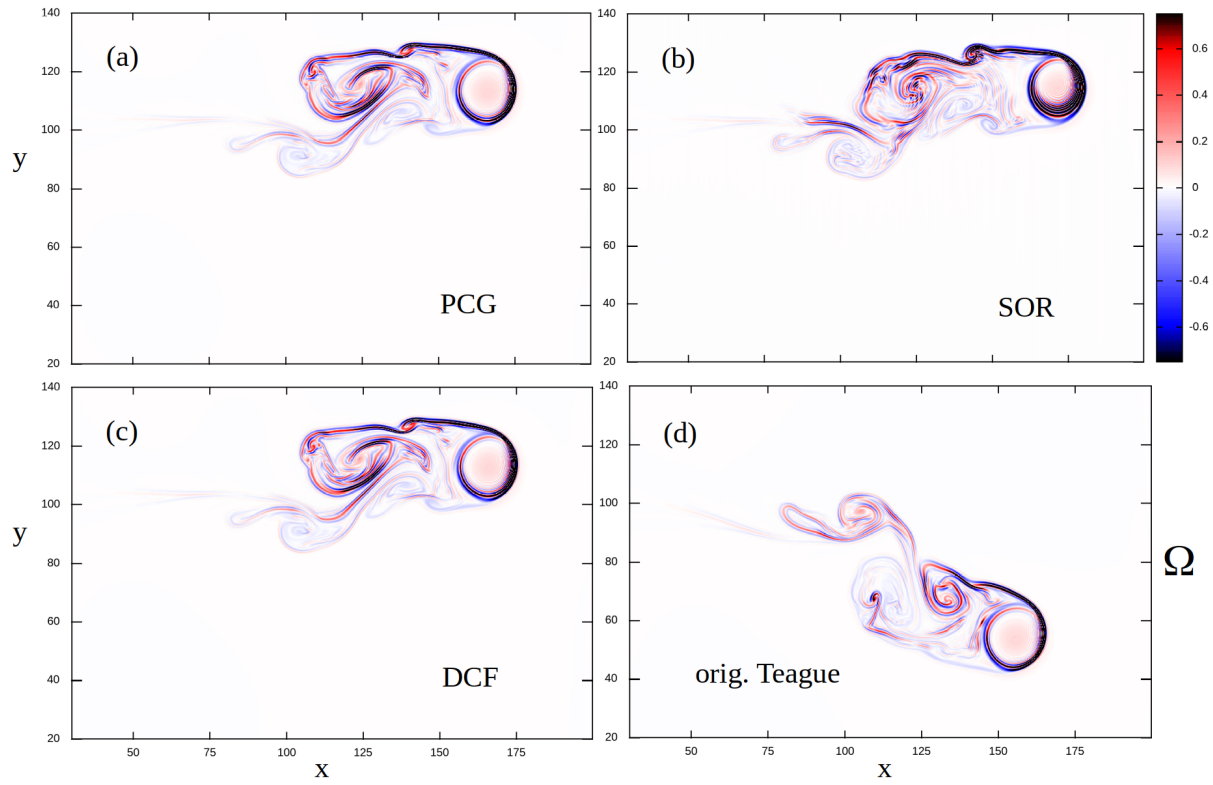


FIG. 5: Comparison of vorticity $\hat{\Omega} = \hat{\boldsymbol{\nabla}}^2\hat{\phi}(x,y)$ for an evolved seeded blob ($\tau_i = 4$, $\hat{N}_0 = 1$, $w = 5$) initialised with $\hat{N}_e = \hat{N}_i$ condition, at $\hat{t} = 2304$, for different generalized Poisson solvers. (a) PCG; (b) SOR; (c) DCF; (d) uncorrected (original) Teague solver.

differ between the code results, because in ref. [59] FELTOR uses a discontinuous Galerkin method with 300 grid cells and 5 polynomial coefficients, which would correspond to 1500 grid points for the TIFF solvers. Overall the agreement between the codes and between the different solvers used in TIFF can be regarded as satisfactory. In particular, the new DCF method has been shown to achieve strong agreement with the other solvers, and in particular with the also fourth order PCG scheme.

The results shown in Fig. 5 have been obtained on a Threadripper PRO 5975WX Linux workstation with 256 GB RAM, running on 32 threads of the CPU. The run time was 216 min with the SOR solver, also 216 min for the PCG solver, 67 min for the DCF solver, and 60 min for the uncorrected Teague solver. The times for the zero vorticity runs (Fig. 4) were 212 min for the SOR solver, 116 min for the PCG solver, and 68 min for the DCF solver, and 59 min for the uncorrected Teague solver. The new DCF solver clearly is most efficient and independent of the complexity of the density fields. The additional cost for the

DCF correction compared to the original Teague method is around 10-15 %.

Shorter run times could of course be achieved for the iterative solvers by reducing accuracy through an increased error tolerance setting. The resolution with 1024^2 grid points could be reduced for practical application scenarios, which would also (for reasons of CFL stability) allow respectively larger time steps: half of the grid points per dimension in 2d thus means roughly 1/8 run time. For specific application to study blob dynamics on a homogeneous background (such as in the verification example above) the code could also be sped up by using only one, physical domain with periodic boundary conditions, instead of the more general quarter-wave extended four-fold mirror domain. This would reduce computation times by another factor of around 4.

IX. DRIFT WAVE TURBULENCE SIMULATIONS IN FULL-F AND FULL-K

The paradigmatic Hasegawa-Wakatani (HW) quasi-2d drift wave turbulence fluid model is in the following extended, as described above, to full-f full-k isothermal gyrofluid simulations. The intention here is again on cross-verification between the polarization solvers. The 2d polarization and gyro operator solvers can be directly implemented in future 3d field-aligned gyrofluid turbulence codes, as the perpendicular (to the magnetic field) 2d drift plane can be solved in the same manner as in a 2d code like here. A 3d (isothermal electrostatic) resistive drift wave turbulence code would basically replace the approximate HW coupling term by direct solution of the parallel electron and ion velocities through an additional set of nonlinear advective dynamical equations.

The morphology of 2d drift wave turbulence in the full-f gyrofluid OHW model is illustrated in Fig. 6 as a snapshot in the saturated turbulent phase, for parameters described below. The left frame shows the electric potential $\phi(x, y)$, which acts as a streamfunction for the advecting turbulent E-cross-B velocity. The right frame shows the vorticity $\Omega(x, y) = \boldsymbol{\nabla}^2\phi$ with the characteristic thin vorticity sheaths induced by FLR spin-up [53].

Fig. 7 shows a radial cut at $y = L_y/2$ of the electron density $n_e(x)$, ion gyrocenter density $n_i(x)$, electric potential $\phi(x)$ and vorticity $\Omega(x)$ at a snapshot in time during the saturated turbulent phase. Radial boundary conditions are set to zero vorticity and zero zonal flow. The densities are pinned to the initial background profiles values at the radial boundaries.

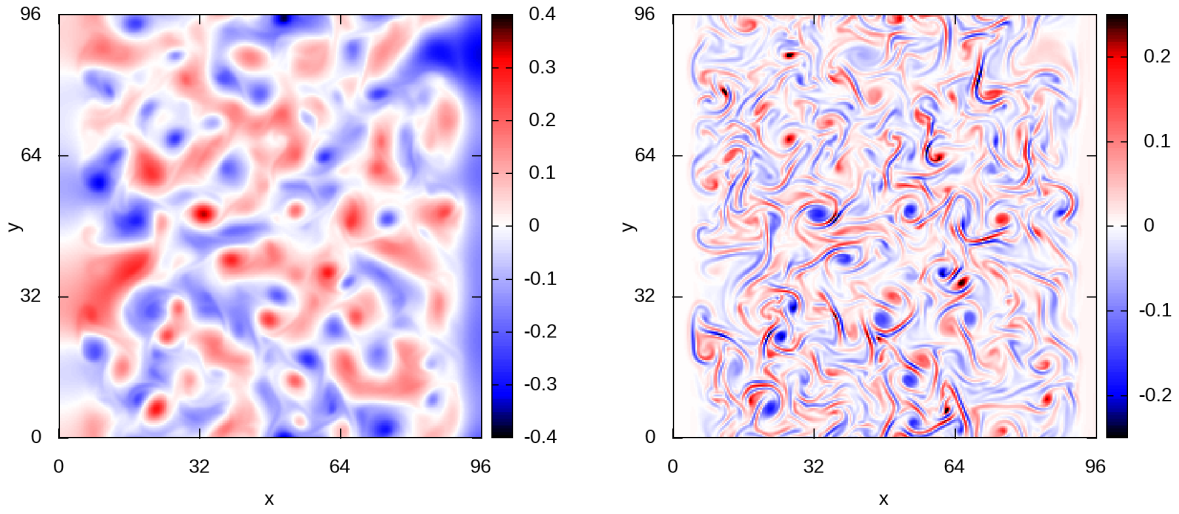


FIG. 6: Snapshots of (left) potential $\phi(x, y)$ and (right) vorticity $\Omega(x, y)$ of drift wave turbulence in the full-f full-k gyrofluid ordinary Hasegawa-Wakatani model, in an $L_x = L_y = 96\rho_s$ domain.

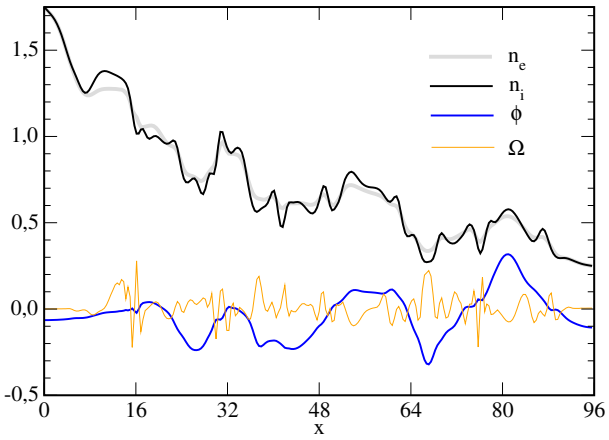


FIG. 7: Radial cut at $y = L_y/2$ of electron density $n_e(x)$, ion gyrocenter density $n_i(x)$, electric potential $\phi(x)$ and vorticity $\Omega(x)$ in the saturated phase of OHW turbulence.

A. Comparison between SOR, PCG and DCF solvers

The different implemented TIFF solvers are compared for an OHW turbulence case with $\hat{\alpha} = 0.2$, $\tau_i = 1$, $\hat{\alpha} = 0.2$, $\kappa = 0$, $\delta = 0.015$, $\hat{N}_L = 1.75$, $\hat{N}_R = 0.25$, $L_x = L_y = 96$, $n_x = n_y = 256$, $\nu_4 = 0.01$, $\Delta t = 0.0025$, and $\beta_x = 2$. Initialisation is done with a random bath of amplitude $\Delta N = 0.05$.

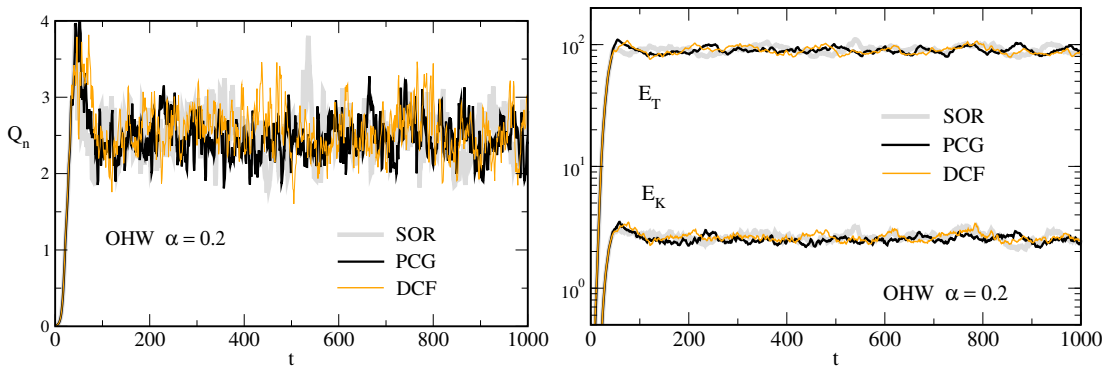


FIG. 8: Comparison of properties for the SOR, PCG and DCF solvers. Left: transport $Q_n(t)$. Right: thermal energy $E_T(t)$ and kinetic energy $E_K(t)$. Turbulent statistical results (averages and deviations) agree closely for all solvers, and accurately in the initial transient quasi-linear phase.

Fig. 8 shows in the left frame the turbulent transport $Q_n(t)$ for the SOR (thick grey), PCG (medium black) and DCF (thin orange) solvers, and in the right the corresponding time traces of thermal energy $E_T(t)$ and kinetic energy $E_K(t)$. All time traces agree closely between the solvers, both in the initial quasi-linear phase and statistically in the turbulent phase. The averages in the time window between $100 \leq t \leq 1000$ are: $\langle Q_n \rangle = 2.50 \pm 0.29$ (SOR), 2.46 ± 0.26 (PCG), 2.55 ± 0.31 (DCF); $\langle E_K \rangle = 2.63 \pm 0.21$ (SOR), 2.50 ± 0.15 (PCG), 2.61 ± 0.18 (DCF); $\langle E_T \rangle = 91.3 \pm 6.2$ (SOR), 89.6 ± 5.0 (PCG), 89.4 ± 6.1 (DCF). The (second order accurate) SOR value of the kinetic energy is around 5 % larger compared to the (fourth order accurate) PCG or DCF results, while the fluctuation standard deviation of energies for all solvers is also in the order of 5 %. The average values of transport and thermal energy agree very well within the standard deviation for all three solvers.

The computation times were 201 min (SOR), 134 min (PCG) and 81 min (DCF), here achieved on 16 threads of a a dual Xeon Haswell E5-2687W-v3 workstation. The (second order) SOR scheme clearly looses in terms of both performance and accuracy compared to the (fourth order) PCG and DCF schemes, but still can have its use for testing purposes as a reference generalized Poisson solver without need for envoking an FFT library.

The new DCF scheme appears to be both sufficiently accurate and efficient to be considered for further use. It should be noted that the 2d FFT evaluation is a memory bound application and profits from high available bandwidth. The relative performance between the solvers can therefore differ between hardware systems.

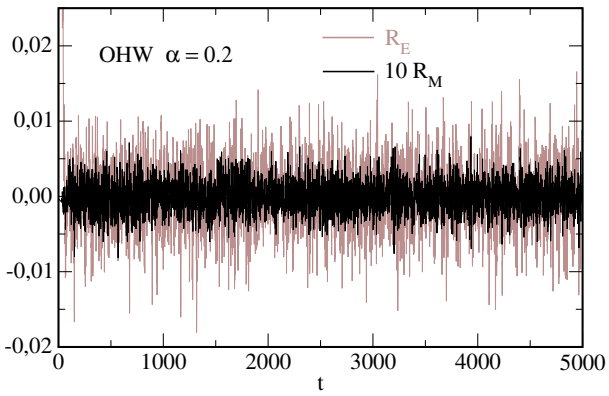


FIG. 9: Conservation of particle number and energy: total energy change rate $R_E = (1/2E)(\Delta E/\Delta t)$ and (ten times magnified) gyrocenter density change rate $R_M = (1/M)(\Delta M/\Delta t)$ as a function of normalized simulation time.

B. Mass and energy conservation test with DCF scheme

Total mass and total energy should always be ideally conserved by the numerical scheme employed for the dynamical turbulence simulation. The change in time of total energy $E(t) = E_K + E_T$ as the sum of the global thermal free energy and the global kinetic energy (see section VI) can be computed as the nonlinear growth rate $R_E = (1/2E)(\Delta E/\Delta t)$, and similar the relative rate of change of particle number (or "mass") is obtained as $R_M = (1/M)(\Delta M/\Delta t)$ for the total gyrocenter density as $M(t) = (1/2)[(\hat{N}_e(t) - \hat{N}_0) + (\hat{N}_i(t) - \hat{N}_0)]$.

These relative energy and mass change rates as a function of time are shown in Fig. 9 for the same turbulence simulation parameters as above, obtained with the DCF scheme. A linear regression for the values in $1000 \leq t \leq 5000$ gives a relative tendency $\langle R_E \rangle(t) \sim 4 \cdot 10^{-6} - 2 \cdot 10^{-10}\, t$ for the energy, and $\langle R_M \rangle(t) \sim \cdot 10^{-8} - 4 \cdot 10^{-10}\, t$ for the particle number. Both constitute very small loss rates and can be regarded as sufficiently good conservation property of the numerical scheme. The standard deviations of the nonlinear growth rate fluctuations are $s(R_E) = 4 \cdot 10^{-3}$ and $s(R_M) = 2 \cdot 10^{-4}$.

C. Full-f model in small amplitude limit vs. delta-f model

The full-f full-k model should agree in the limit of small amplitudes with the delta-f model, as discussed in sections IV B and VII. To test this we apply largely the same parameters as above to OHW simulations with the DCF solver: $\hat{\alpha} = 0.2$, $\tau_i = 1$, $\kappa = 0$,

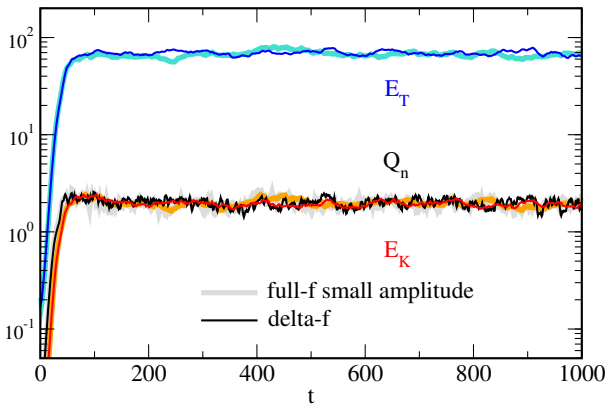


FIG. 10: Comparison of the full-f full-k model in the small amplitude limit with the corresponding delta-f model, for an OHW ($\hat{\alpha} = 0.2$) turbulence simulation. The transport $Q_n(t)$, thermal energy $E_T(t)$ and kinetic energy $E_K(t)$ agree closely, both in the quasi-linear transient growth phase, and statistically in the nonlinear turbulent phase after around $t > 150$.

$\nu_4 = 0.01$, $L_x = L_y = 96$, $n_x = n_y = 256$, and $\Delta t = 0.0025$. The inner boundary density is $\hat{N}_L = 1 + \epsilon \cdot 0.75$ and outer boundary density $\hat{N}_R = 1 - \epsilon \cdot 0.75$, with drift scale $\delta = \rho_s / L_n = \epsilon \cdot 0.015$. A localized "blob"-like Gaussian perturbation with width $w = 8$ and amplitude $\Delta\hat{N} = \epsilon \cdot 0.1$ is initialised. This parameter set is once run with the delta-f model of section VII for $\epsilon = 1$, and once with the complete full-f model but for $\epsilon = 10^{-3}$ in the small amplitude limit.

In Fig. 10 the time traces of $Q_n(t)$, $E_T(t)$ and $E_K(t)$ are compared for both cases. They show excellent agreement both directly in the quasi-linear growth phase, and statistically in the nonlinear turbulent phase after around $t > 150$. Averages in the time window between $200 \leq t \leq 1000$ are: $\langle Q_n \rangle = 1.95 \pm 0.21$ (FF-ϵ) vs. 1.97 ± 0.20 (δf); $\langle E_K \rangle = 1.96 \pm 0.15$ (FF-ϵ) vs. 1.93 ± 0.11 (δf); $\langle E_T \rangle = 67.6 \pm 4.7$ (FF-ϵ) vs. 69.6 ± 3.6 (δf).

This demonstrates the correct transition behaviour of the full-f full-k polarization equation and the dynamical equations towards the delta-f limit. The computation time here was about twice as long (81 min) for the full-f simulation than for the delta-f case (41 min) on the Haswell. The computational expense is in the evaluation of the Fourier solvers (in the polarization and for the gyro operators), for which there are eight calls in the full-f DCF case, and four in the delta-f case.

X. CONCLUSIONS AND OUTLOOK

An isothermal quasi-2d gyrofluid model and a code (TIFF) for arbitrary amplitude (full-f) and arbitrary wavelength (full-k) drift instabilities and turbulence in magnetized plasmas has been introduced. A major aspect was on testing of a here newly suggested "dynamically corrected Fourier" (DCF) solver for the generalized Poisson equation, which is based on the original approximate Teague method. The generalized (a.k.a. "variable") Poisson problem appears in the solution of the gyrofluid (similar to the gyrokinetic) polarization equation, which couples the evolving gyrocenter plasma densities with the electric potential. The present approach retains the complete FLR effects and spatial and dynamical variations of the polarization density. The new DCF solver was shown to be a viable, sufficiently accurate and efficient method for dynamical turbulence simulations coupled to the generalized Poisson problem, which motivates its further use in future extensions of the code.

In its recursive "RCF" form (with for example four iteration) as a high accuracy extension of Teague's method the scheme could also find applications in the field of optics as a stand-alone application for solution of the transport of intensity equation (TIE).

The main purpose of the present work is as reference and test case for the TIFF model and code, whereas detailed physics studies with the present code, such as for example on FLR effects on zonal flows, or on properties of turbulently generated "blobby" (intermittent) transport, will be discussed elsewhere.

The extension of the 2d TIFF code to a magnetic field-aligned flux-tube like 3d geometry can directly make use of the here tested polarization solvers, as these always only act in the locally perpendicular 2d drift plane. Future developments of such a corresponding 3d full-f full-k gyrofluid edge turbulence code will include the addition of temperature evolution equations (and through this applicability on temperature gradient driven modes and use of Landau damping mechanisms), and generalization to electromagnetic drift-Alfvén dynamics.

Acknowledgment

The author thanks Markus Held (UiT / UIBK) and Matthias Wiesenberger (DTU) for valuable discussions and collaboration.

Funding

This work was supported by the Austrian Science Fund (FWF) project P33369.

Data availability

The code TIFF is openly available at: https://git.uibk.ac.at/c7441036/tiff

Appendix A: PCG scheme

Conjugate gradient methods for the solution of linear systems are introduced in numerical textbooks such as by LeVeque [75]. Here a pre-conditioned conjugate gradient (PCG) scheme, with a pre-conditioner and algorithm suggested by Fisicaro et al. [77], is applied.

A generalized Poisson operator $\mathcal{A} \equiv \boldsymbol{\nabla} \cdot \varepsilon \boldsymbol{\nabla}$ is defined so that a solution of the system $\mathcal{A}\phi = \sigma$ is sought. The residual of an approximate solution $\phi^{(n)}$, say obtained in step n during an iteration, is $r^{(n)} = \sigma - \mathcal{A}\phi^{(n)}$. Within the context of a dynamical simulation with small time steps Δt, an initial guess can be obtained by extrapolating the converged solutions from previous time steps towards

$$\phi^{(0)}(t) = \phi(t-1) + a \cdot [\phi(t-1) - \phi(t-2)], \tag{31}$$

with a free estimation factor $a \in (0, 1)$, and $\phi^{(0)}(t = 0) = 0$ in the first time step. From this the initial residual $r^{(0)} = \sigma - \mathcal{A}\phi^{(0)}$ for the iteration is obtained.

The PCG scheme basically searches for the minimum of a (quadratic) residual function $f(\phi) = (1/2)(\phi, \mathcal{A}\phi) - (\phi, \sigma)$, which is given from a 2d Hessian Taylor expansion, by evaluating its (conjugate) gradients $\boldsymbol{\nabla} f(\phi) = r = \sigma - \mathcal{A}\phi$. Here $(A, B) = A^T B = \sum_{i,j} A_{i,j} B_{i,j}$ denotes the inner product of two matrices A and B. A pre-conditioning matrix $q^{(0)}$ is evaluated once (in each dynamical time step) and remains constant throughout the PCG iteration.

The iteration algorithm (cf. sec. 5.3.5 in ref. [75], and table 2 in ref. [77]) proceeds as:
(0) Pre-process $q^{(0)} \equiv \sqrt{\varepsilon} \boldsymbol{\nabla}^2 \sqrt{\varepsilon}$.
(1) $v^{(n)} \equiv \mathcal{P}^{-1}(r^{(n)})$, with a precondition operator $\mathcal{P}$ specified below.
(2) $\beta^{(n)} = (v^{(n)}, r^{(n)})/(v^{(n-1)}, r^{(n-1)})$, for $n \neq 0$.
(3) $p^{(n)} = v^{(n)} + \beta^{(n)} p^{(n-1)}$.

(4) $w^{(n)} = \mathcal{A}p^{(n)} = \mathcal{A}v^{(n)} + \beta^{(n)}\mathcal{A}p^{(n-1)} = r^{(n)} - q^{(0)}v^{(n)} + \beta^{(n)}w^{(n-1)}$.

(5) $\alpha^{(n)} = (v^{(n)}, r^{(n)})/(p^{(n)}, w^{(n)})$.

(6) $\phi^{(n+1)} = \phi^{(n)} + \alpha^{(n)}p^{(n)}$.

(7) $r^{(n+1)} = r^{(n)} - \alpha^{(n)}w^{(n)}$.

(8) Return to step (1) until the residual $||r^{(n+1)}||$ is below a specified limit.

The algorithm allows to efficiently re-use several already calculated terms and products. A classical conjugate gradient (CG) solver without preconditioning of the residual in step (1) would set $\mathcal{P} = 1$ and $v^{(n)} = r^{(n)}$ in the algorithm. The idea is that a preconditioned residual $v = \mathcal{P}^{-1}r = \mathcal{P}^{-1}\sigma - \mathcal{P}^{-1}\mathcal{A}\phi$ is minimized in the same way as the original r.

Application of a suitable preconditioner can speed up convergence significantly, but needs to be chosen carefully. Here the preconditioner suggested in ref. [77] for the generalized Poisson problem is applied as $\mathcal{P}() \equiv \sqrt{\varepsilon}\boldsymbol{\nabla}^2\sqrt{\varepsilon}()$, and accordingly $q^{(0)} \equiv \sqrt{\varepsilon}\boldsymbol{\nabla}^2\sqrt{\varepsilon}$ above.

The evaluation of $\mathcal{A}v = \boldsymbol{\nabla}\cdot\varepsilon\boldsymbol{\nabla}v = \sqrt{\varepsilon}\boldsymbol{\nabla}^2 v\sqrt{\varepsilon} - v\sqrt{\varepsilon}\boldsymbol{\nabla}^2\sqrt{\varepsilon} = \mathcal{P}(v) - vq^{(0)} = r - vq^{(0)}$ in step (4) is greatly simplified by this preconditioner [77]. For the inversion in step (1) here $v^{(n)} = \mathcal{P}^{-1}(r^{(n)}) = (1/\sqrt{\varepsilon})\boldsymbol{\nabla}^{-2}(r^{(n)}/\sqrt{\varepsilon})$ needs to be evaluated including the application of a standard fast Poisson solver, which is here presently achieved by an FFT solver in $\mathbf{k}$ space. The additional expense of calling a standard Poisson ($\boldsymbol{\nabla}^2 u = f$) solver at each iteration step is paid off by the in general rapid convergence of this PCG scheme. The default choice for the standard Poisson solver in the TIFF code is by FFT, but optionally also a (generally slower) SOR scheme is available. The order of this PCG solver is determined by the order of evaluation of the Laplacians (in $q^{(0)}$, or in a non-FFT standard Poisson solver), which is here achieved in fourth order accuracy.

The algorithm above could also be converted into a (preconditioned) steppest descent scheme by setting $\beta^{(n)} = 0$, which more serves didactical than practical purposes because of its generally slower convergence.

Appendix B: SOR scheme

Successive over-relaxation (SOR) is an established method for iterative solution of elliptic equations, such as the generalized Poisson equation $\boldsymbol{\nabla}\cdot\varepsilon\boldsymbol{\nabla}\phi = \sigma$ of electrostatics, through an appropriate finite difference discretization. Here a basic algorithm and second order discretization as outlined in the textbooks by LeVeque [75] and Humphries [76] is followed.

In one dimension, the inner term $\varepsilon\partial_x\phi \approx W\ \Delta\phi/\Delta x$ is first discretized with interpolated coefficients $W = (\varepsilon_i+\varepsilon_{i-1})/2$, and $\Delta\phi = \phi_i-\phi_{i-1}$. In the following an equidistant rectangular grid with $\Delta x = \Delta y \equiv h$ is assumed. Applying likewise the outer derivative, one gets $W_{i+1}(\phi_{i+1}-\phi_i) - W_{i-1}(\phi_i-\phi_{i-1}) = h^2\sigma$, with coefficients $W_{i+1} = (\varepsilon_{i+1}+\varepsilon_i)/2$ and $W_{i-1} = (\varepsilon_i+\varepsilon_{i-1})/2$, which can be re-arranged to define ϕ_i at grid node x_i.

In the same manner, the 2d relation for $\phi_{i,j}$ in 2nd order 5pt-stencil is obtained as

$$\begin{aligned}\phi_{i,j} \;=\; \frac{1}{W_0}\,(&W_{i+1,j}\phi_{i+1,j} + W_{i-1,j}\phi_{i-1,j} + \\ &+W_{i,j+1}\phi_{i,j+1} + W_{i,j-1}\phi_{i,j-1} - h^2\sigma_{i,j}\big)\end{aligned} \tag{32}$$

with $W_0 = W_{i+1,j} + W_{i-1,j} + W_{i,j+1} + W_{i,j-1}$, and $W_{i+1,j} = (\varepsilon_{i+1,j}+\varepsilon_{i,j})/2$, $W_{i-1,j} = (\varepsilon_{i-1,j}+\varepsilon_{i,j})/2$, $W_{i,j+1} = (\varepsilon_{i,j+1}+\varepsilon_{i,j})/2$, $W_{i,j-1} = (\varepsilon_{i,j-1}+\varepsilon_{i,j})/2$.

Starting with an initial guess $\phi^0(\mathbf{x})$, the relation (32) can be iterated, with grid values of $\phi^{(n)}_{i,j}$ applied on the r.h.s. in order compute the updated $\phi^{(n+1)}_{i,j}$ on the left, until the residual error norm $||R^{(n+1)}||$ with $R^{(n+1)} = \phi^{(n+1)} - \phi^{(n)}$ is smaller than a specified limit.

The SOR method [75] improves convergence by applying a correction factor ω as

$$\phi^{(n+1)} = \phi^{(n)} + \omega R^{(n)}. \tag{33}$$

The grid array is swept in odd ("red") - even ("black") order, as in eq. (32) the values of $\phi^{(n)}_{i,j}$ for even indices i or j depend only on odd indexed grid values of $\phi^{(n-1)}$, and vice versa. The over-relaxation parameter ω is determined by Chebyshev acceleration according to $\omega^0_{odd} = 1$ and $\omega^0_{even} = 1/(1-r^2/2)$ as initial values, and further $\omega = 1/(1-r^2\omega/4)$, updated in each half-sweep. Here the spectral radius is calculated as $r = [\cos(\pi/n_x) + \cos(\pi/n_y)]/2$ for a homogeneous equidistant grid with grid point numbers n_x and n_y. Each "red" and "black" sweep through the 2d checkerboard-like grid is loop parallelized with OpenMP, respectively.

Convergence can be significantly accelerated by an initial guess for $\phi^0(\mathbf{x})$ based on the solution from previous time step(s) within a dynamical simulation for small time steps Δt, by extrapolating (in similar spirit as for the over-relaxation factor above)

$$\phi^0 \equiv \phi(t-1) + a\cdot(\phi(t-1) - \phi(t-2)). \tag{34}$$

with a free prediction factor $a \in (0,1)$. The first time step uses $\phi^0 = 0$, in the second step $a = 0$, and in later times a factor between 0.5 and 1.0 has been found to be most efficient.

The rate of convergence depends on the degree of (non)uniformity of $\varepsilon(\mathbf{x})$. In classical electrostatics the permittivity is usually only weakly varying within one medium, but may have discontinuities between neighbouring media, and is often set in complicated geometries, so that mostly rather finite element schemes instead of finite difference schemes are employed. In the present application on the gyrofluid polarization equation in a small local section of an edge plasma, the grid can be simply chosen as rectangular, but the polarization density can be strongly inhomogeneous for large amplitude turbulent fluctuations.

The present SOR implementation is only second order accurate, but straightforward to implement and can serve as a reference for the fourth order PCG and DCF schemes. For consistency, all dynamical simulations shown in this publication that have been obtained with the second order SOR scheme also use the second order versions of the Arakawa scheme (for the advecting Poisson brackets) and of the curvature operator. For all other generalized Poisson sovers (DCF, PCG) the respective consistent fourth order versions are used.

For evaluation of the standard Poisson problem ($\boldsymbol{\nabla}^2 u = f$) also a fourth order accurate SOR scheme is available in the TIFF code, which uses discretization by a Collatz Mehrstellenverfahren (9pt stencil for the Laplacian on u, and a 5pt stencil correction for f).

Appendix C: DCF scheme

The here introduced "dynamically corrected Fourier" (DCF) approach for the generalized Poisson problem adds a correction term, computed from the result of the previous time step within a dynamical simulation, to "Teague's method" (compare main text above). Teague's approximate method [69] had originally been devised for solution of the TIE (transport of intensity equation) in optics [70], and can be efficiently evaluated in Fourier space [71].

It is here innovatively applied on solution of the electric potential $\phi(\mathbf{x})$ from the gyrofluid (or gyrokinetic) polarization equation, and within a dynamical context. For small time step sizes Δt this allows to re-use solutions of ϕ^{old} from past times, instead of a (more expensive) iterative error correction. An extrapolated prediction with a free estimation parameter $a \in (0, 1)$ based on two previous solutions is used for the corrector, as

$$\phi^{old} \equiv \phi^{(t-1)} + a \cdot (\phi^{(t-1)} - \phi^{(t-2)}). \tag{35}$$

The generalized Poisson equation $\boldsymbol{\nabla} \cdot \varepsilon \boldsymbol{\nabla} \phi = \sigma$ is formulated by means of a polarization

density vector field $\mathbf{P} \equiv \varepsilon \boldsymbol{\nabla}\phi \equiv \boldsymbol{\nabla} p + \boldsymbol{\nabla} \times \mathbf{H}$ in terms of a scalar potential p and a vector potential $\mathbf{H} = \eta\, \mathbf{e}_z$. Input quantities are the known 2d fields $\sigma(\mathbf{x})$ and $\varepsilon(\mathbf{x})$.

By application of the divergence on $\boldsymbol{\nabla} \cdot \mathbf{P} = \sigma$ the scalar field p is first obtained from:

$$p = \boldsymbol{\nabla}^{-2}\sigma. \tag{36}$$

The inversion of the Laplacian in the standard Poisson problem is here obtained in $\mathbf{k}$ space by Fourier transforms, using the FFTW3 library, as $p = -\mathcal{F}^{-1}k^{-2}\mathcal{F}\sigma$.

Further, an approximation for A is obtained (see main text above) from $\boldsymbol{\nabla} \times \mathbf{P}$ as:

$$\eta_o(\mathbf{x}) \equiv \boldsymbol{\nabla}^{-2}\{\phi^{old}, \varepsilon\}. \tag{37}$$

This estimated quantity is used in the extended, dynamically corrected relation:

$$\phi(\mathbf{x}) = \boldsymbol{\nabla}^{-2}\left[\boldsymbol{\nabla} \cdot \frac{1}{\varepsilon}\boldsymbol{\nabla} p + \left\{\frac{1}{\varepsilon}, \eta_o\right\}\right]. \tag{38}$$

Like above, the inverted Laplacians in eqs. (37) and (38) can be efficiently solved in Fourier space. The term $\boldsymbol{\nabla} \cdot (1/\varepsilon)\boldsymbol{\nabla} p$ is evaluated by standard (fourth order) centered finite differences, and the Poisson bracket can be computed either also by simple fourth order centered differences, or by re-using the Arakawa scheme (introduced for the advective terms in the dynamical gyrocenter density equations).

For a solver unit test (with a constructed solution) the set of equations (37) and (38) can also be applied recursively (instead of within a dynamical context) by re-setting $\phi \to \phi^{old}$ directly after each iteration step, starting with $\eta_o = 0$. In the main text above this is refered to as "RCF" for recursively corrected Fourier scheme.

The computational bottleneck in this DCF solver for the generalized Poisson equation is provided by the three forward plus backward 2d Fourier transforms (in the three $\boldsymbol{\nabla}^{-2} = -\mathcal{F}^{-1}k^{-2}\mathcal{F}$ operations). To put this in context, note that in addition, Fourier solvers are here presently also used for evaluation of all gyro-operators: application of any (PCG, SOR or DCF) solver on the full-k polarization equation requires two further, here also Fourier based, evaluations of the $\sqrt{\Gamma_0}^{-1}$ operator (in TIFF code algorithm steps #4 and 5), and in general another in computing $\hat{N}_{Gi}$ for use in σ in step #2, one more for the ion potential ϕ_i, and a further one in the boundary conditions (step #4). In total eight forward plus backward transforms are employed per time step. The execution time per Fourier solver application depends only on the size of the grid arrays (and the chosen transform method or library),

which by extrapolation allows predictable run time estimates. For cold ion cases ($\tau_i = 0$) without FLR effects the four gyro-operations herein can be bypassed, and computation time is significantly reduced.

For comparison, the delta-f polarization equation requires only one call of a Fourier solver routine (regardless of cold or warm ions) for a given σ, so the execution time for a full-f full-k polarization solve is more than five times longer compared to a delta-f solution. (When iterative solvers such as PCG or SOR are used, the execution time could be tweaked by compromising on accuracy.)

References

[1] G.R. Tynan, A. Fujisawa, and G. McKee. Plasma Physics and Controlled Fusion 51, 113001 (2009).

[2] B. Scott, Turbulence and instabilities in magnetized plasmas: fluid drift turbulence. Volume 1. IOP Publishing, Bristol (2021).

[3] B. Scott, Turbulence and instabilities in magnetized plasmas: gyrokinetic theory and gyrofluid turbulence. Volume 2. IOP Publishing, Bristol (2021).

[4] G. Knorr, F.R. Hansen, J.P. Lynov, H.L. Pécseli, and J.J. Rasmussen. *Physica Scripta* **38**, 829 (1988)

[5] G. W. Hammett, W. Dorland, and F. W. Perkins. Physics of Fluids B 4, 2051 (1992).

[6] W. Dorland and G. Hammett, *Phys. Fluids B* **5**, 812 (1993).

[7] M.A. Beer and G.W. Hammett, *Phys. Plasmas* **3**, 4046 (1996).

[8] P.B. Snyder and G.W. Hammett, Physics of Plasmas **8**, 3199 (2001).

[9] B.D. Scott, Physics of Plasmas **7**, 1845 (2000).

[10] B.D. Scott, Physics of Plasmas **12**, 102307 (2005).

[11] A. Kendl, B.D. Scott, and T.T. Ribeiro, Physics of Plasmas 17, 072302 (2010).

[12] B.D. Scott, Contributions to Plasma Physics **46**, 714 (2006).

[13] B.D. Scott, Physics of Plasmas **14**, 102318 (2007).

[14] B.D. Scott, Physics of Plasmas **17**, 102306 (2010).

[15] B.D. Scott, A. Kendl and T. Ribeiro, Contributions to Plasma Physics **50**, 228 (2010).

[16] D. Strintzi and B. Scott, *Phys. Plasmas* **11**, 5452 (2004).

[17] D. Strintzi and B. Scott, *Phys. Plasmas* **12**, 072301 (2005).

[18] J. Madsen, Phys. Plasmas **20**, 072301 (2013).

[19] W.W. Lee, Physics of Fluids **26**, 556 (1983).

[20] T.S. Hahm, Physics of Fluids **31**, 2670 (1988).

[21] H. Sugama, Physics of Plasmas **7**, 466 (2000).

[22] A.J. Brizard and T.S. Hahm, Reviews of Modern Physics **79**, 421 (2007).

[23] B. Scott and J. Smirnov, Physics of Plasmas **17**, 112302 (2010).

[24] J A. Krommes, Annual Review of Fluid Mechanics **44**, 175 (2012).

[25] B. Scott, Contributions to Plasma Physics **56**, 534 (2016).

[26] M. Endler, H. Niedermeyer, L. Giannone, E. Kolzhauer, A. Rudyj, G. Theimer and N. Tsois, Nuclear Fusion **35**, 1307 (1995).

[27] S.J. Zweben, J.A. Boedo, O. Grulke, C. Hidalgo, B. LaBombard, R.J. Maqueda, P. Scarin and J.L. Terry, Plasma Physics and Controlled Fusion **49**, S1-S23 (2007).

[28] J.A. Heikkinen, S.J. Janhunen, T.P. Kiviniemi, F. Ogando, Journal of Computational Physics **27**, 5582 (2008).

[29] V. Grandgirard, Y. Sarazin, P. Angelino, A. Bottino, N. crouseilles, G. Darmet, G. Dif-Pradalier, X. Garbet, Ph. Gendrih, S. Jolliet, G. Latu, E. Sonnendrücker and L. Villard, Plasma Physics and Controlled Fusion **49**, B173 (2007).

[30] S. Ku, C. S. Chang and P. H. Diamond, Nuclear Fusion **49**, 115021 (2009).

[31] M.A. Dorf, M.R. Dorr, J.A. Hittinger, R.H. Cohen and T.D. Rognlien, Physics of Plasmas **23**, 056102 (2016).

[32] V. Grandgirard, J. Abiteboul, J. Bigot, T. Cartier-Michaud, N. Crouseilles, G. Dif-Pradalier, Ch. Ehrlacher, D. Esteve, X. Garbet, Ph. Gendrih, G. Latu, M. Mehrenberger, C. Norscini, Ch. Passeron, F. Rozar, Y. Sarazin, E. Sonnendrücker, A. Strugarek, D. Zarzoso, Computer Physics Communications **207**, 35 (2016).

[33] Y. Idomura, M. Ida, T. Kano, N. Aiba and S. Tokuda, Computer Physics Communications **179**, 391 (2008).

[34] Y. Idomura, Physics of Plasmas **21**, 022517 (2014).

[35] Q. Pan, D. Told, E. L. Shi, G. W. Hammett and F. Jenko, Physics of Plasmas **25**, 062303 (2018).

[36] E.L. Shi, G.W. Hammett, T. Stoltzfus-Dueck and A. Hakim, Physics of Plasmas **26**, 012307 (2019).

[37] D. Michels, A. Stegmeir, P. Ulbl, D. Jarema and F. Jenko, Computer Physics Communications **264**, 107986 (2021).

[38] M. Held, *Full-F gyro-fluid modelling of the tokamak edge and scrape-off layer*, PhD Thesis, Universität Innsbruck (2017), urn:nbn:at:at-ubi:1-6853, http://diglib.uibk.ac.at/ulbtirolhs/download/pdf/1530595.

[39] M. Wiesenberger and M. Held, *Feltor V.6.* feltor-dev.github.io, Zenodo, https://doi.org/10.5281/zenodo.6201099.

[40] M. Wiesenberger, L. Einkemmer, M. Held, A. Gutierrez-Milla, X. Sáez, R. Iakymchuk, Computer Physics Communications 238, 145-156 (2019)

[41] M. Wiesenberger, J. Madsen, A. Kendl, Phys. Plasmas **21**, 092301 (2014)

[42] M. Held, M. Wiesenberger, J. Madsen, A. Kendl, Nuclear Fusion **56** 126005 (2016).

[43] M. Held, M. Wiesenberger, R. Kube, A. Kendl Nuclear Fusion **58** 104001 (2018).

[44] M. Held, M. Wiesenberger, A. Kendl, Nuclear Fusion **59**, 026015 (2019).

[45] B. Scott, New Journal of Physics **4**, 52.1 (2002).

[46] B. Scott, Plasma Phys. Control. Fusion **45**, A385 (2003).

[47] T.T. Ribeiro, B. Scott, Plasma Phys. Control. Fusion **50**, 055007 (2008).

[48] A. Kendl, International Journal of Mass Spectrometry **365/366**, 106 (2014).

[49] O.H.H. Meyer, A. Kendl, Plasma Phys. Control. Fusion **58**, 115008 (2016).

[50] O.H.H. Meyer, A. Kendl, Plasma Phys. Control. Fusion **59**, 065001 (2017).

[51] O.H.H. Meyer, A. Kendl, Nuclear Fusion **57**, 126066 (2017).

[52] A. Kendl, Physics of Plasmas **19**, 112301 (2012).

[53] A. Kendl, Plasma Phys. Control. Fusion **60**, 025017 (2018).

[54] A. Kendl, Plasma Phys. Control. Fusion **57**, 045012 (2015).

[55] A. Kendl, G. Danler, M. Wiesenberger, M. Held, Physical Review Letters **118**, 235001 (2017).

[56] A. Kendl, Physics of Plasmas **25**, 102111 (2018).

[57] E. Reiter, M. Wiesenberger, M. Held, G.W. Zarate-Segura, A. Kendl, Journal of Plasma Physics **89**, 905890110 (2023).

[58] M. Held, M. Wiesenberger, A. Kendl, Nuclear Fusion **60**, 066014 (2020).

[59] M. Held, M. Wiesenberger, Nuclear Fusion **63**, 026008 (2023).

[60] A. Hasegawa, M. Wakatani, Physics of Plasmas **14**, 102312 (2007).

[61] R. Numata, R. Ball and R.L. Dewar, Physics of Plasmas **14**, 102312 (2007).

[62] F.D. Halpern, P. Ricci, S. Jolliet, J. Loizu, J. Morales, A. Mosetto, F. Musil, F. Riva, T. M. Tran, C. Wersal, Journal ofComputational Physics **315** 388 (2016).

[63] B.D. Dudson, J. Leddy, Plasma Phys. Control. Fusion **59**, 054010 (2017).

[64] J. Madsen, V. Naulin, A.H. Nielsen, J.J. Rasmussen, Physics of Plasmas **23**, 032306 (2016).

[65] M. Frigo, and S.G. Johnson, Proceedings of the IEEE **93** (2), 216-231 (2005).

[66] A. Arakawa, J. Comput. Phys. **1**, 119 (1966).

[67] V. Naulin, A. Nielsen, SIAM J. Sci Comput. **25**, 104 (2003).

[68] G.E. Karniadakis, M. Israeli, S.A. Orszag, J. Comput. Phys. **97**, 414 (1991).

[69] M.R. Teague, Journal of the Optical Society of America **73**, 1434 (1983).

[70] C. Zuo, J. Li, J. Sun, Y. Fan, J. Zhang, L. Lu, R. Zhang, B. Wang, L. Huang, Q. Chen, Optics and Lasers in Engineering **135**, 106187 (2020).

[71] D. Paganin, K.A. Nugent, Physical Review Letters **80**, 2586 (1998).

[72] J.A. Schmalz, T.E. Gureyev, D.M. Paganin, K.M. Pavlov, Physical Review E **84**, 023808 (2011).

[73] J.A. Ferrari, G.A. Ayubi, J.L. Flores, C.D. Perciante, Optics Communication **318**, 133 (2014).

[74] C. Zuo, Q. Chen, L. Huang, A. Asundi, Optics Express **22**, 17172 (2014).

[75] R.J. LeVeque, *Finite difference methods for ordinary and partial differential equations.* SIAM, Philadelphia, 2007.

[76] S. Humphries, *Field solution on computers.* CRC Press, 1997. Electronic version (2010): http://www.fieldp.com/femethods.html

[77] G. Fisicaro, L. Genovese, O. Andreussi, N. Marzari, S. Goedecker, The Journal of Chemical Physics **144**, 014103 (2016).